Surface-Wave Tomography of the Central-Western Mediterranean: New Insights Into the Liguro-Provençal and Tyrrhenian Basins

Fabrizio Magrini[1,2] , Giovanni Diaferia[1] , Amr El-Sharkawy[3,4] , Fabio Cammarano[1] , Mark van der Meijde[5] , Thomas Meier[3], and Lapo Boschi[6,7,8]

[1]Department of Sciences, Università degli Studi Roma Tre, Roma, Italy, [2]Institute of Geosciences, Johannes Gutenberg University of Mainz, Mainz, Germany, [3]Christian Albrechts Universität, Kiel, Germany, [4]National Research Institute of Astronomy and Geophysics (NRIAG), Cairo, Egypt, [5]Faculty of Geo-Information Science and Earth Observation (ITC), University of Twente, Enschede, The Netherlands, [6]Dipartimento di Geoscienze, Università degli Studi di Padova, Padua, Italy, [7]Sorbonne Université, CNRS, INSU, Institut des Sciences de la Terre de Paris, Paris, France, [8]Istituto Nazionale di Geofisica e Vulcanologia, Bologna, Italy

Abstract The complex tectonic setting of the central-western Mediterranean has interested geoscientists for decades, but its geodynamic evolution remains a matter of debate. We rely on 807 seismometers from southern Europe and northern Africa to measure Rayleigh and Love phase velocities in the period range ∼5–200 s, based on teleseismic earthquakes and seismic ambient noise. By nonlinear joint inversion of the phase-velocity maps, we obtain a 3-D shear-wave velocity (V_s) model of the study area. At shallow depths, our model correlates with surface geology and reveals the presence of a sedimentary cover in the Liguro-Provençal basin, as opposed to the Tyrrhenian basin where this is either very thin or absent. At ∼5-km depth, high velocities below the Magnaghi, Vavilov, and Marsili seamounts point to an exhumed, scarcely serpentinized mantle. These are replaced by lower velocities at larger depths, likely connected to the presence of partial melt. At 50–60-km depth, a very heterogeneous structure characterizes the Tyrrhenian basin, with low velocities pointing to the presence of fluids due to the lateral mantle inflow from the Ionian slab edges, and higher velocities associated with a relatively dry upper mantle. Such heterogeneity disappears at depths ≳75 km, replaced by more uniform velocities which are ∼2% lower than those found in the Liguro-Provençal basin. We infer that, at the same depths, the Tyrrhenian basin is characterized by a larger concentration of fluids and possibly higher temperatures.

Plain Language Summary The Mediterranean area has long been considered by geoscientists as a source of inspiration for understanding geodynamic processes on a global scale, but its deep structure remains a matter of debate. We rely on seismic data from 807 receivers distributed across southern Europe and northern Africa to measure surface-wave (Rayleigh and Love) phase velocities, based on both strong earthquakes and seismic ambient noise. We use these observables to obtain an improved shear-velocity model of the central-western Mediterranean, covering the Liguro-Provençal and the Tyrrhenian basins. The shallow features of our model are consistent with known geological structures, and indicate a thick sedimentary cover in the Liguro-Provençal basin which is absent beneath the Tyrrhenian Sea. At larger depths (∼50–60 km), we find a very heterogeneous structure in the Tyrrhenian basin, as opposed to the more uniform Liguro-Provençal basin. The observation is consistent with a relatively high concentration of fluids in the south-eastern part of the Tyrrhenian basin at the same depths, which can be ascribed to the subduction of the Ionian slab beneath Calabria. Our results are discussed in light of recent geodynamic models, with a focus on the role of slab dynamics in controlling the compositional character of back-arc basins.

1. Introduction

The Mediterranean area has long been considered by Earth scientists as a source of inspiration for understanding the dynamics that slowly shape our planet. Its complexity is evidence of past and present geodynamic evolution, and makes it a *natural laboratory* for studying the processes that govern the Earth's interior (for a review, see, e.g., Faccenna et al., 2014). Its formation can be ascribed to the motion, collision, and subduction of several microplates, which constitute a dynamic patchwork extending over the whole region. The convergence of the African and Eurasian plates, started in the late Mesozoic, led to the subduction of the Tethys Ocean beneath
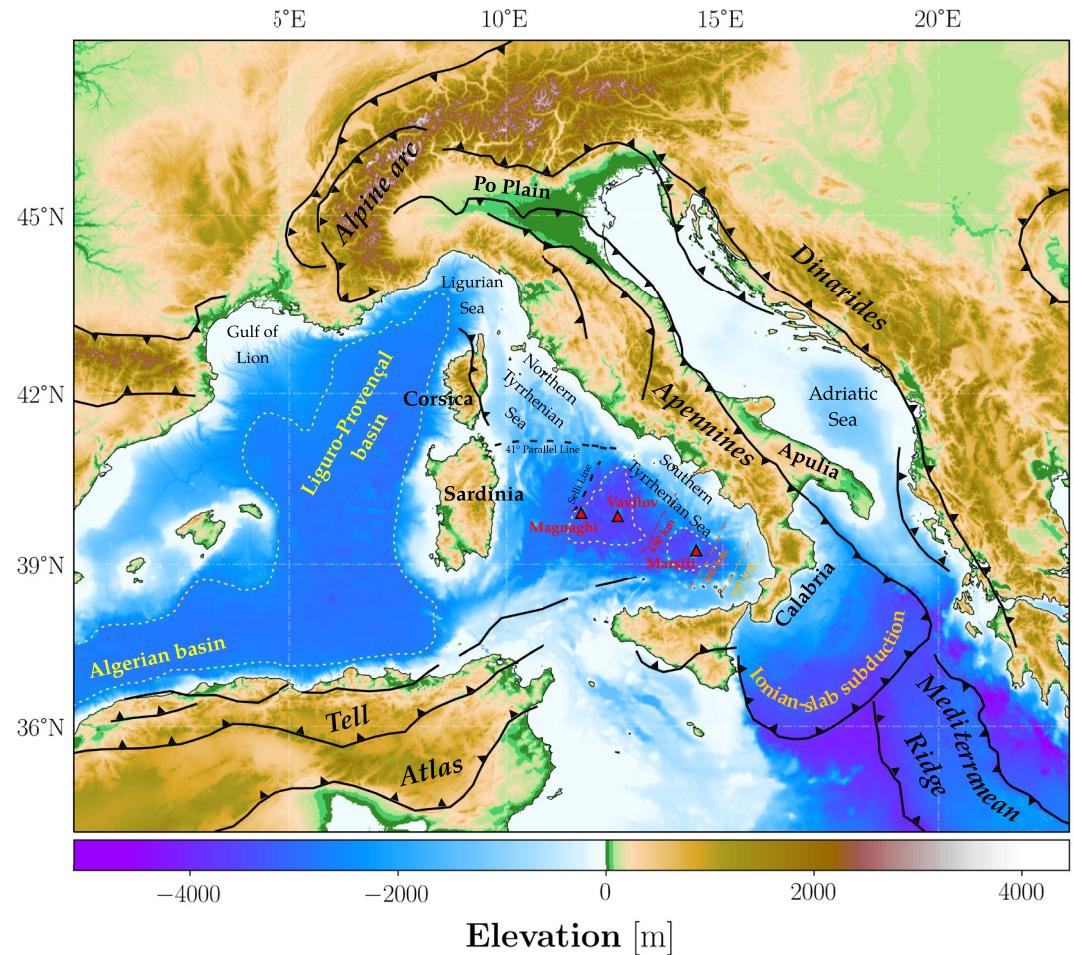
Figure 1. Major faults (modified from Faccenna et al. (2014)) and topography/bathymetry (denoted by the background color) of the study area. Magnaghi, Vavilov, and Marsili seamount locations are indicated by the red triangles. Yellow dashed lines identify the Magnaghi-Vavilov, the Marsili, and the Liguro-Provençal basin as reported by Faccenna et al. (2014). Modified after Gvirtzman and Nur (1999), the colored dashed lines in the southern Tyrrhenian Sea indicate the depth of the Ionian slab, subducting beneath the region.

Eurasia, e.g., to the uplift of the Alpine belt, and to the formation of Apennines and Dinarides. The central-western Mediterranean alone, focus of the study, is characterized by the presence of (a) the formerly much larger Adriatic plate, that is subducting to the west beneath the Apennines and to the east beneath the Dinarides and Hellenides, (b) relatively young, mainly Neogene western Mediterranean back-arc basins, and (c) very old Triassic oceanic lithosphere that is subducting beneath Calabria, commonly referred to as Ionian slab (Figure 1). In this complex tectonic setting, the central-western Mediterranean features two small oceanic basins: the Liguro-Provençal and the Tyrrhenian basin.

The formation of the Liguro-Provençal basin has been much debated, but ultimately ascribed to the separation of the Sardinia-Corsica continental block from the southern European paleo-margin (actual France/Spain), and subsequent counterclockwise rotation (e.g., Faccenna et al., 2001; Gattacceca & Speranza, 2002). This process would have been triggered by an extensional event ~30 Ma (e.g., Faccenna et al., 2002, 2004). The Tyrrhenian basin, instead, is a marine basin that can be subdivided in its northern and southern parts by the 41° Parallel line (Figure 1), a tectonic lineament which has been interpreted as a major strike-slip fault system (Rosenbaum & Lister, 2004). The southern part of the Tyrrhenian Sea is of great interest to geoscientists. It represents a back-arc basin that started to open in recent times (~12-10 Ma) in response to the trench retreat of the Ionian slab, currently active below Calabria (e.g., Chiarabba & Palano, 2017; Faccenna et al., 2004). Even more recently (since ~6 Ma), this part of the Mediterranean underwent a new extension phase, oriented NW-SE, triggered by

the tearing and rapid rollback of the Adriatic slab (subducting beneath the Italian peninsula). Altogether, these dynamics led to the present bathymetry of the southern Tyrrhenian Sea, punctuated by volcanoes and seamounts, that testify an intense history of deformation associated with ongoing emplacement of oceanic lithosphere (e.g., Wortel & Spakman, 2000). Among these seamounts, it is worth mentioning the Magnaghi and Vavilov, which define the Magnaghi-Vavilov basin (bounded at north-west by the Selli line), and the Marsili, associated with the homonymous basin (Figure 1).

Despite the interest that the Mediterranean area has generated among geoscientists for decades, the seismic structure of the upper mantle beneath Liguro-Provençal and Tyrrhenian Sea is still largely unknown. This can be ascribed to scarcity of seismic receivers across the Sardinia-Corsica continental block, that limited the resolution of previous tomographic models (see, e.g., Greve et al., 2014; Manu-Marfo et al., 2019). This study is motivated by the recent installation of the LiSard (Lithosphere of Sardinia) seismic array, consisting of 10 broadband receivers deployed between June 2016 and September 2018 in 11 different locations across Sardinia. Given its position, this island represents a strategical outpost to ensure a good illumination of both the Liguro-Provençal and Tyrrhenian basin.

Previous investigations based on LiSard-array data have been limited, so far, to few surface-wave studies on Sardinian and Corsican crust and lithospheric mantle (i.e., Boschi et al., 2019, 2020; Magrini et al., 2020b). Here, we join the LiSard data with all the publicly available seismograms recorded across the central-western Mediterranean between 1990 and 2018 (Figure 2). To obtain seismic images of the study area, we rely on Rayleigh and Love waves generated by both teleseismic events and seismic ambient noise (henceforth AN). Earthquake-based (EQ) and AN data contain complementary information, and their joint use results in a data set sensitive to a broad depth range (e.g., Ritzwoller et al., 2011; Zhou et al., 2012). Based on pairs of receivers, we first use these recordings to compute Rayleigh and Love fundamental-mode phase velocities in the period range ∼5–200 s (Section 2). From the dispersion curves, we then obtain Rayleigh and Love phase-velocity maps via a linearized inversion based on ray theory (Section 3). Finally, we jointly invert the phase-velocity maps to obtain a 3-D shear-wave velocity (V_S) model, using the neighborhood algorithm (Section 4). Our tomographic model extends to depths of 200 km, and is discussed in Section 5 with the aid of several depth slices and cross-sections.

2. Rayleigh and Love Dispersion Curves

2.1. AN Phase Velocities

We measured AN phase velocities from continuous three-component seismograms. These have been recorded between July 2016 and October 2018 at 512 receivers distributed across the study area (Figure 2). The time window used for the download maximizes the overlapping between the recordings of the LiSard array and those of the other seismic networks; this ensures a good seismic coverage on both the Liguro-Provençal and the Tyrrhenian basins. Each seismogram has been demeaned, detrended, tapered (5%), and bandpass filtered between 0.01 and 0.5 Hz before deconvolving with the instrument response to get displacement. Based on the preprocessed waveforms, we retrieved fundamental-mode Rayleigh (vertical and radial) and Love interstation phase velocities by means of an automated algorithm (Kästle et al., 2016). In practice, for each station pair, we first subdivide their simultaneous recordings in overlapping (50%) 1-h-long time windows, and cross-correlate them in the frequency domain. The resulting cross-correlations are then ensemble averaged to obtain a unique cross-spectrum. This is compared to the zeroth order Bessel function of the first kind $J_0 \left(\frac{\omega \Delta}{c} \right)$, associated with the considered interstation distance Δ and angular frequency ω. True phase velocity $c = c(\omega)$ can then be found considering that $J_0 \left(\frac{\omega \Delta}{c(\omega)} \right)$ will be in phase with the observed cross-spectrum (Aki, 1957; Ekström et al., 2009). The cross-correlations are performed on vertical-component recordings, to obtain the velocity of vertically polarized Rayleigh waves, and on the horizontal components (radial and transverse, respectively) for radially polarized Rayleigh waves and Love waves.

The data set thus obtained covers a broad period range (∼5–200 s), and consists of 98,252 Rayleigh-wave dispersion curves (55,749 associated with the vertical component, 42,503 with the radial), and 50,746 Love-wave dispersion curves (Figure 3). We assessed the uncertainty of the AN measurements using the "method of the triplets" (Lin et al., 2008). This method consists of identifying triplets of receivers approximately lying on the same great circle path (we set a maximum azimuthal deviation of 1°). For each triplet, at a given period,
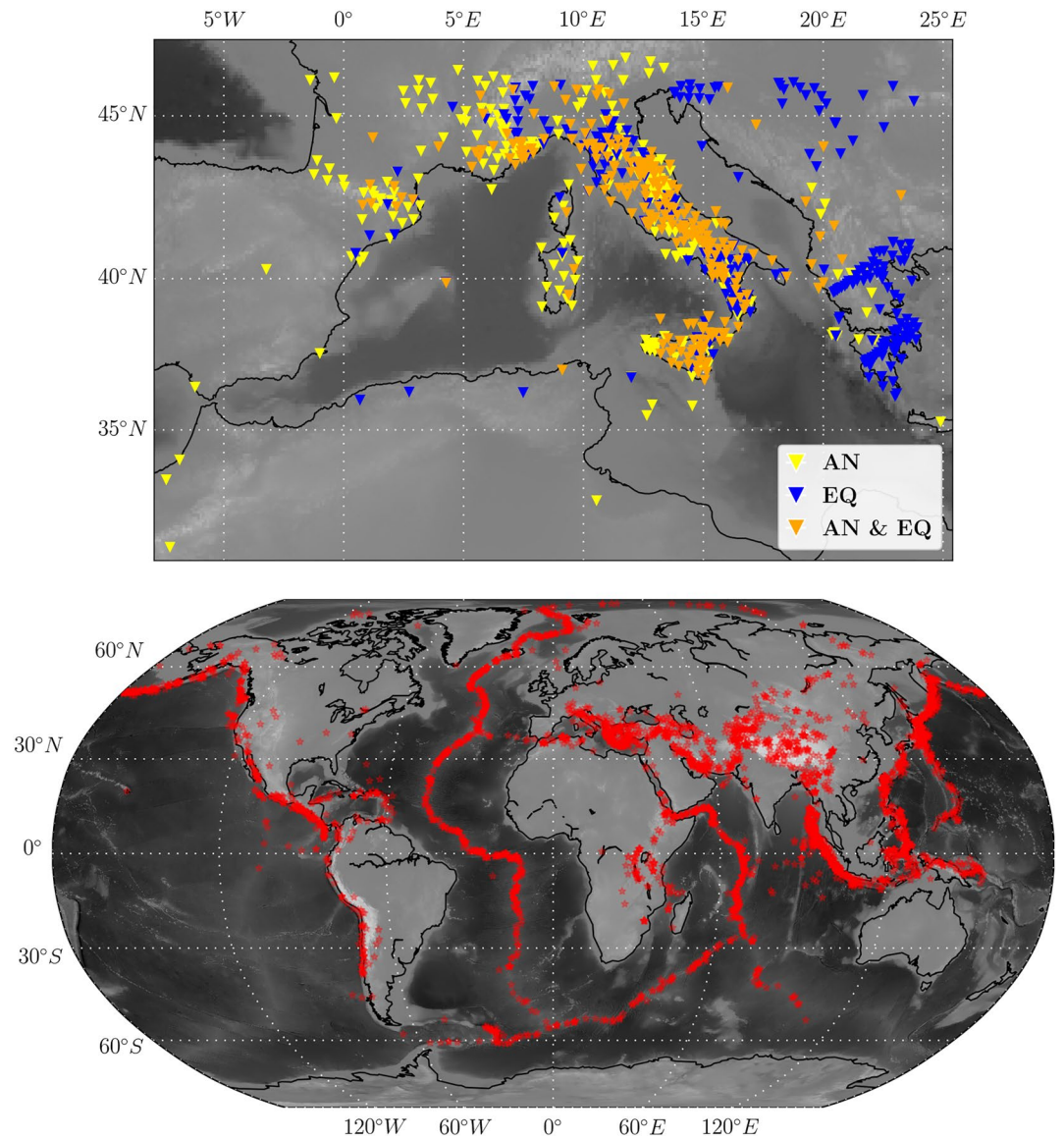
Figure 2. (top) Location of the seismic receivers (triangles) used in this study. Overall, we relied on 807 seismic stations: 271 for computing only dispersion curves based on seismic ambient noise (AN, yellow), 295 for earthquake-based ones (EQ, blue), and 241 for both AN and EQ (orange). (bottom) Epicenters of the 3,823 seismic events (red stars) used to retrieve EQ phase velocities.

the phase velocity associated with the most distant pair is compared to the other two (e.g., Kästle et al., 2018; Lin et al., 2008; Magrini et al., 2020b). Different weights are assigned to the phase velocities associated with each triplet, to account for small deviations from the great circle path passing through the three stations (Lin et al., 2008). Velocity differences observed at each triplet can be ascribed to errors in the AN measurements, and their distribution can be used to assess the uncertainty on the dispersion curves at different surface-wave periods. We find that, compared to the vertical component, radial-component and transverse-component dispersion curves are characterized by larger errors and uncertainties; these, however, are relatively small at all periods, as illustrated in Figure S1 in Supporting Information S1 associated with this paper.
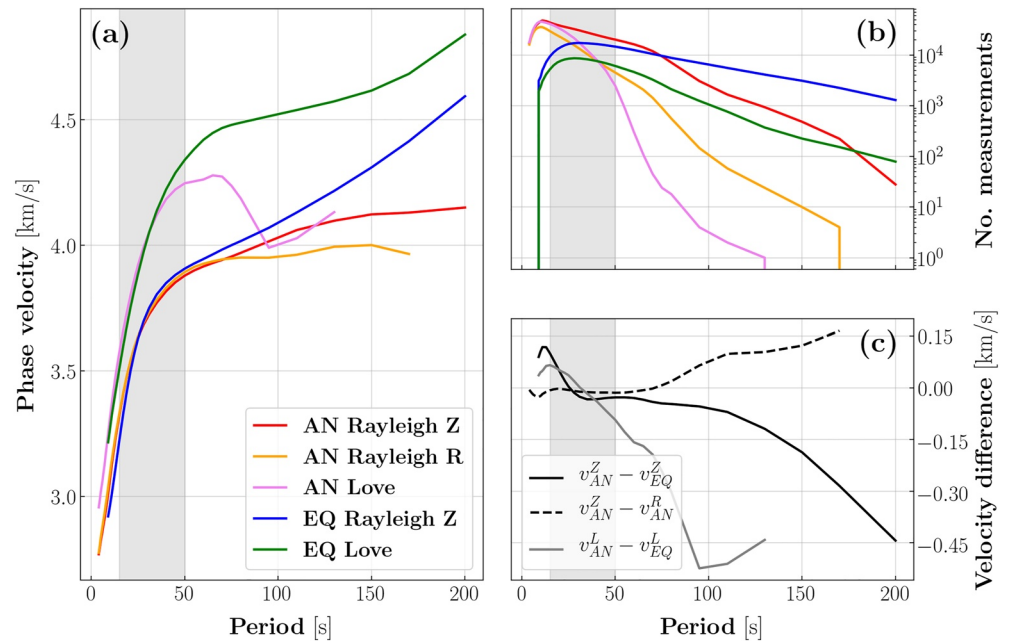
Figure 3. (a) Average phase-velocity measurements retrieved from AN and EQ recordings. Measurements obtained from vertical-component (Z) recordings of Rayleigh waves are shown in red and blue for AN and EQ, respectively; those associated with Love waves are colored in pink and green; in orange, AN measurements obtained from the radial (R) components. The number of measurements as a function of period is shown in (b), using the same colors as (a). Average velocity differences between the vertical components of AN and EQ ($v_{AN}^Z - v_{EQ}^Z$, black solid line), between vertical and radial components of AN ($v_{AN}^Z - v_{AN}^R$, black dashed line), and between Love-wave measurements ($v_{AN}^L - v_{EQ}^L$, gray line) are shown in panel (c). In each subplot, the region shaded in gray indicates the period range in which AN and EQ phase velocities are used jointly in the inversion to phase-velocity maps; at shorter (longer) periods only AN (EQ) measurements are used in the inversion, as explained in Section 3.1.

2.2. EQ Phase Velocities

We computed fundamental-mode Rayleigh and Love phase velocities through the automated algorithm of Soomro et al. (2016), exploiting 3,823 teleseismic events recorded at 536 receivers between 1990 and 2015 (Figure 2). As in El-Sharkawy et al. (2020), the minimum magnitude of the earthquakes is chosen to vary linearly as a function of the epicentral distance, between 4 (at 2.7°) and 6 (at 120°). The two-station algorithm of Soomro et al. (2016) exploits the phase delay observed at pairs of receivers approximately aligned on the same great circle path as the epicenter (we set the maximum azimuthal deviation to 7°). The phase delay is calculated via filtered and weighted cross-correlations, and used to retrieve the frequency-dependent phase velocity through the dispersion relation (e.g., Magrini et al., 2020a; Meier et al., 2004), i.e., $c = \frac{\omega x}{\phi}$, where ω, x, and ϕ denote angular frequency, inter-station distance, and phase delay, respectively. We measure Rayleigh-wave phase velocities by cross-correlating vertical-component recordings, and Love-wave ones using the transverse components.

Analogous to Soomro et al. (2016), only those parts of the dispersion curves fulfilling strict quality criteria are accepted. These include (a) a maximum deviation of 15% from a reference dispersion curve, (b) the smoothness of phase velocity as a function of frequency, and (c) a length criterion that rejects relatively short (and therefore not well constrained) segments of dispersion curves. For each station pair, the final dispersion curve is calculated as an average of the accepted phase-velocity measurements associated with at least five earthquakes. To obtain robust measurements, those associated with less than five events or with relatively large standard deviations (here, >2% of the average velocity at a given period) are discarded.

The above procedure resulted in 32,123 dispersion curves (20,994 for Rayleigh waves, 11,127 for Love), whose average values are shown in Figure 3a to be in agreement with those obtained from AN data in the period range 15–50 s. Outside this period range, AN and EQ dispersion curves show relatively large differences, which are particularly prominent at periods >50 s (Figure 3c). Such a systematic bias has been observed in previous
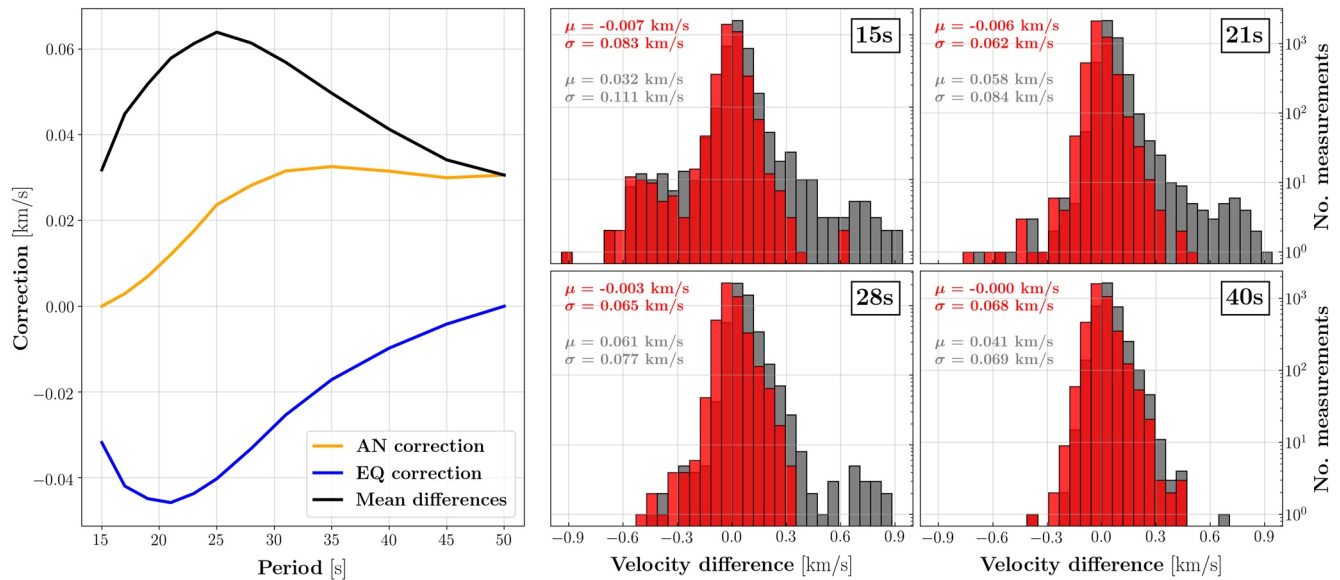
Figure 4. (left) Illustration of the velocity correction as a function of period applied to AN (orange) and EQ (blue) Rayleigh-wave dispersion curves. At each period, the relative amount of the correction is determined by a weighting function $w(\omega)$ and by the average velocity difference $\mu(\omega)$ (black) between the two data sets, calculated through the station pairs for which both EQ and AN dispersion curves are available (as $v_{EQ} - v_{AN}$). (right) Distribution of the phase-velocity differences between EQ and AN at different periods (15, 21, 28, and 40 s) before applying the correction (gray histograms) and after the correction (red). Within each subpanel, mean (μ) and standard deviation (σ) of the distributions are reported on the left. Note the significant decrease of the bias between EQ and AN after application of the correction.

studies (e.g., Kästle et al., 2016; Magrini et al., 2020a) and can be probably ascribed to the difficulty of AN interferometry to retrieve robust measurements at periods much longer than those of the primary microseism band, i.e., ~10–20 s (e.g., Friedrich et al., 1998). At shorter periods, small differences between EQ and AN can in principle be explained by deviations in the wave propagation path between earthquake and receivers, due to lateral heterogeneity in the Earth's structure (Magrini et al., 2020a). Alternatively, previous authors suggested that differences in AN versus EQ sensitivity kernels (e.g., Fichtner et al., 2016), overtone contamination (e.g., Soomro et al., 2016), or low signal-to-noise-ratio in the AN cross-correlations (e.g., Kästle et al., 2016) may contribute to the observed bias.

3. Phase-Velocity Maps

3.1. Correction of the Systematic Bias Between AN and EQ

Before translating the dispersion curves to maps, we made a selection of the phase velocities to exclude from the AN and EQ data sets those measurements which we do not consider robust. To do that, we restricted the span of the period range of the dispersion curves: in light of the considerations above, we discarded AN phase velocities at periods >50 s and EQ measurements at periods <15 s. In other words, in the inversion to phase-velocity maps, AN and EQ dispersion curves are used jointly only in the period range 15–50 s, characterized by relatively small velocity differences (Figure 3c).

We then applied a correction to each measurement falling in this period range, based on the average velocity difference between the two data sets (calculated through the station pairs for which both EQ and AN dispersion curves are available); this is done to further reduce the observed bias between EQ and AN, as illustrated in Figure 4. In practice, at different periods, we defined a correction term that is function of the average velocity difference $\mu(\omega)$ and of a weighting function $w(\omega)$, where ω denotes frequency. The correction term $\mu(\omega)w(\omega)$ is added to v_{AN}, where v is phase velocity, while $\mu(\omega)(w(\omega) - 1)$ is added to v_{EQ}. The weighting function $w(\omega)$ is chosen to increase logarithmically between 0 (at 15 s) and 1 (at 50 s); consequently, at a given period, if $\mu(\omega)$ $w(\omega)$ is positive (and therefore v_{AN} is increased), $\mu(\omega)(w(\omega) - 1)$ will be negative (and v_{EQ} will be decreased), and vice versa. This prior correction allows for taking into account the variability, as a function of period, in the

confidence of the measurements, with AN being more "reliable" at 15 s and EQ being more "reliable" at 50 s. We carried out the above procedure for Rayleigh and Love dispersion curves separately. As a result, the systematic bias between AN and EQ measurements is practically zeroed, and the standard deviation of the velocity difference distributions decreased (Figure 4).

3.2. From Dispersion Curves to Phase-Velocity Maps

We inverted the corrected dispersion curves for Rayleigh and Love phase-velocity maps at different periods (Figures 5 and 6) using an iterative linear-least-squares inversion based on the ray theory. This algorithm was first developed by Boschi and Dziewonski (1999) and then modified by Schaefer et al. (2011), who implemented the option of an adaptive spatial parameterization. The algorithm first defines an equal-area grid covering the region of interest. In the areas characterized by a relatively high density of interstation paths, it then refines the parameterization by splitting each grid cell into four subblocks. Here, we meshed the study area using equal-area blocks of $1.6° \times 1.6°$; at a given period, all grid cells intersected by >100 paths are iteratively refined up to a maximum number of three times, i.e., up to a maximum spatial resolution of 0.2°. The resulting parameterization of the Rayleigh and Love phase-velocity maps is illustrated in Figures S2 and S3 in Supporting Information S1, respectively, together with the number of interstation paths intersecting each grid cell.

The inversion consists of finding the minimum least squares solution of the inverse problem

$$\begin{bmatrix} \mathbf{A} \\ \mu\mathbf{G} \end{bmatrix} \cdot \mathbf{x} = \begin{bmatrix} \mathbf{d} \\ \mathbf{0} \end{bmatrix} \tag{1}$$

(Boschi & Dziewonski, 1999; Lu et al., 2018), where $\mathbf{A} \cdot \mathbf{x} = \mathbf{d}$ is the ill-conditioned forward problem, $\mu\mathbf{G} \cdot \mathbf{x} = \mathbf{0}$ the regularization term, and bold characters denote vector notation. In practice, the inversion is set up, at different periods, with station-pairs' coordinates (used to compute the matrix $\mathbf{A}$) and corresponding time-delays $\mathbf{d}$; the time-delays are calculated from the phase velocities using the average velocity observed at each period as a reference model. The inversion is regularized using a roughness damping constraint, weighted by the scalar μ that we chose, at each period, via L-curve analysis (e.g., Hansen, 1999). To ensure that the different data sets (e.g., AN-radial, AN-vertical, EQ) contribute equally in determining the result of the inversion at a given period, different weights are attributed to their dispersion curves; this is achieved by multiplying both sides of the forward-problem equation by a weight vector $\mathbf{w}$. Specifically, $\mathbf{w}$ is defined by setting the weight of the largest data set to 1, while the others are given a higher weight in proportion to their size with respect to the largest. In addition, we downweighted the AN-radial measurements by 25% at all periods, because of the greater noisiness that typically characterizes the waveforms recorded on the radial components compared to the vertical (e.g., Kästle et al., 2018).

The resulting phase-velocity maps (Figures 5 and 6) are smooth at all periods, and present features that can be related to known geologic domains, as discussed in Section 5.

3.3. Resolution Test

To assess the resolution of the phase-velocity maps we performed a "checkerboard test," illustrated in Figure 7. We first generated synthetic data at different periods using a synthetic velocity model and applying the forward-problem equation, i.e., $\mathbf{d}_{synth} = \mathbf{A} \cdot \mathbf{x}_{synth}$. The model $\mathbf{x}_{synth}$ is characterized by velocity anomalies of $\pm10\%$ with respect to the average velocity observed in the real data at each period, and their spatial extent is approximately equal to the average wavelength (Figure 7). Following exactly the same procedure explained in Section 3.2, we then inverted the synthetic data $\mathbf{d}_{synth}$ thus generated to retrieve the input model $\mathbf{x}_{synth}$.

This test allowed us to verify how well our dispersion curves are able to constrain the velocity variations across the study area. From a visual inspection of Figure 7, it turns out that the resolution on the Italian peninsula and on the European continent is very good at all periods, due to a relatively high density of receivers. The ability of our dispersion measurements to resolve the Liguro-Provençal basin, the Tyrrhenian, and the Adriatic Sea is limited at the shorter, more attenuated periods (e.g., at 5 s); this can be ascribed to the lack of ocean-bottom seismometers

Rayleigh
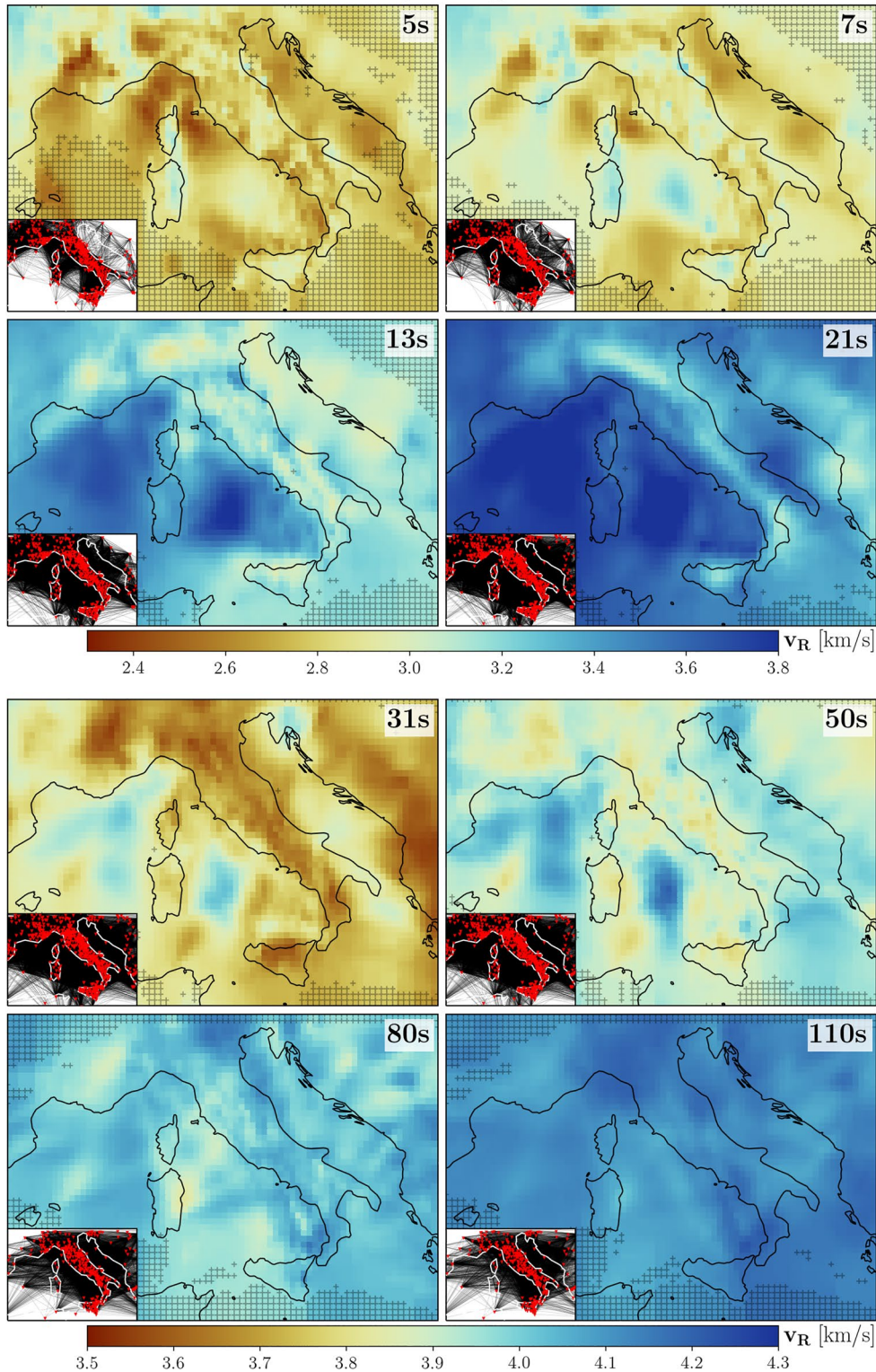
Figure 5. Rayleigh-wave phase-velocity maps at different periods. Colors are associated with two different palettes, one used for shorter periods (5, 7, 13, and 21 s), the other for longer periods (31, 50, 80, and 110 s). Within each subplot, the seismic coverage on the study area is shown at the lower bottom, in the form of great circle paths (black) connecting the station pairs (red triangles) for which dispersion curves are available. Gray crosses indicate, at each period, the pixels intersected by less than five ray paths.

Love
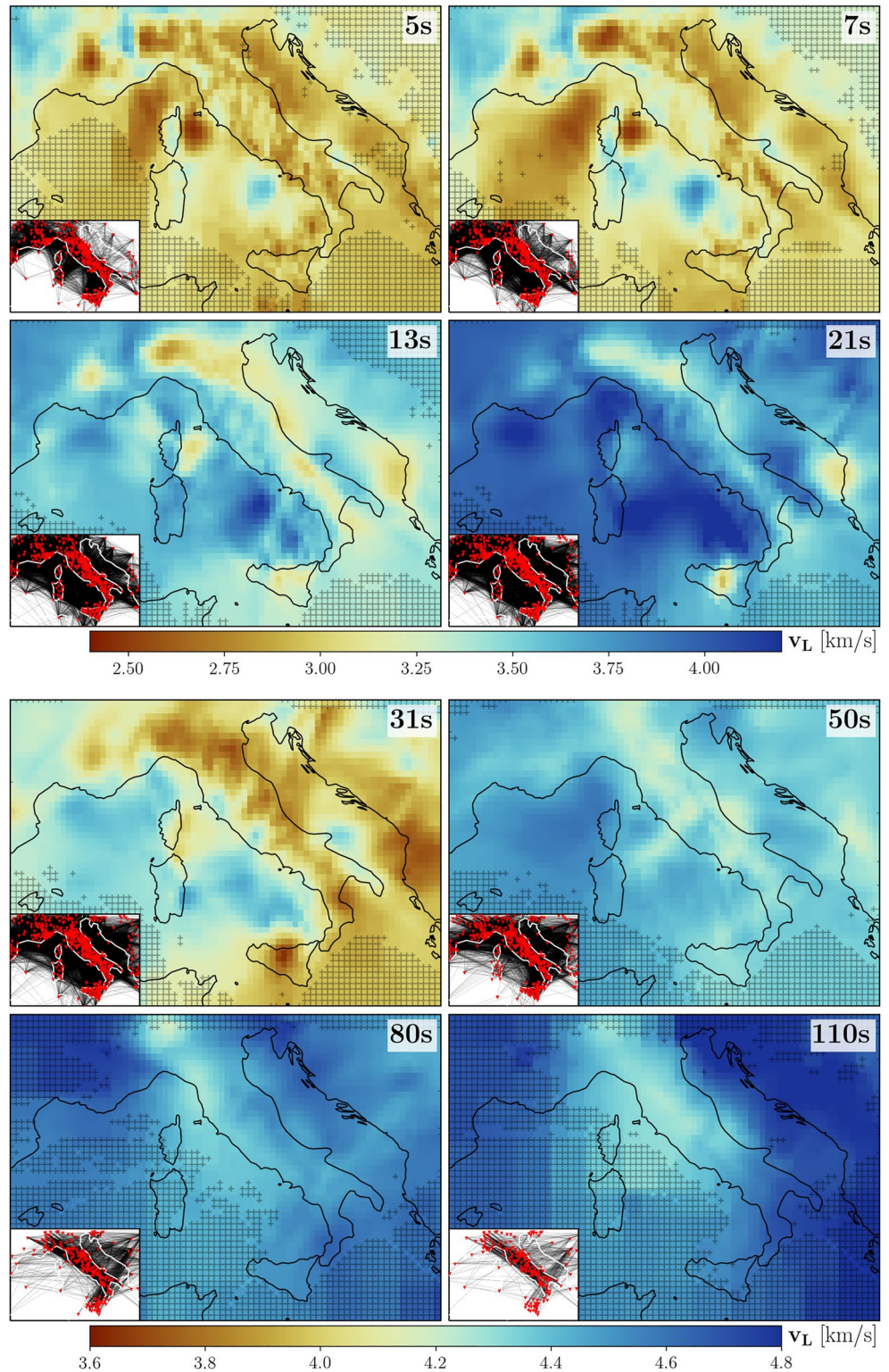
Figure 6. Same as Figure 5, but obtained from Love-wave phase-velocity measurements.

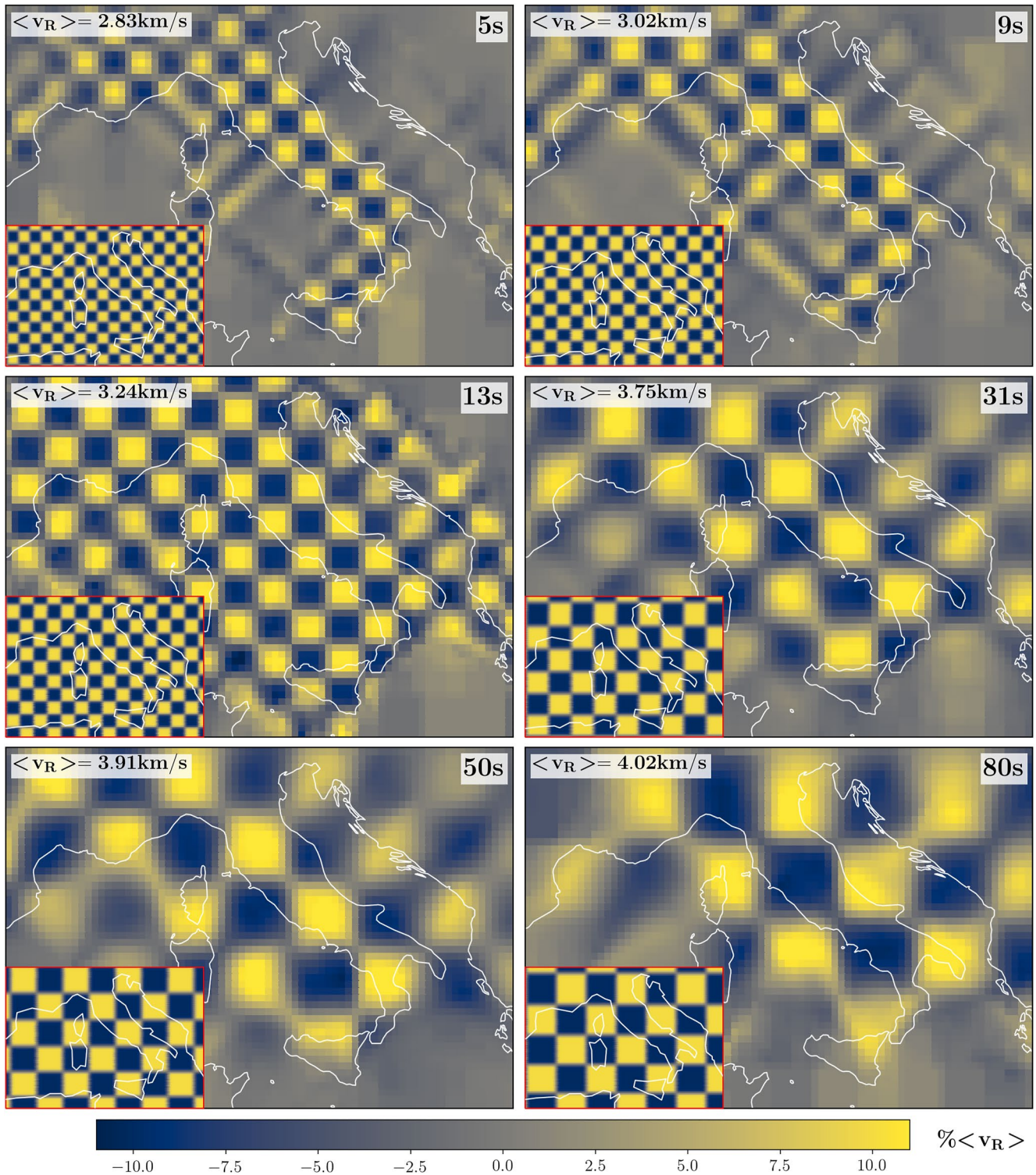**Figure 7.** Results of the checkerboard test shown at the periods of 5, 9, 13, 31, 50, and 80 s. Within each subpanel, the synthetic model used to generate synthetic data is shown on the bottom left. The lateral variations in velocity are expressed as ±10% with respect to the average velocity observed in the real data, indicated on the upper left of each panel.

Table 1
Boundary Conditions Used in the Inversion to V_S Through the Neighborhood Algorithm

Layer	Bottom depth/thickness (km)	V_P (km/s)	V_S (km/s)	Density (g/cm^3)	Velocity gradient
Sedimentary	$0.1 - 12$ (depth)	1.6–6.8	0.8–3.0	2.400	Linear increase
Upper crust	$0.5 - d_E - 25\%$ (depth)	5.0–7.2	2.5–4.0	2.750	Linear increase
Lower crust	$4 - d_E + 25\%$ (depth)	5.0–7.2	3.0–4.2	2.900	Linear increase
Moho (d_M)					
Mantle 1	$(220 - d_M) \times 0.25$	7.3–8.6	4.0–4.95	3.370	Linear
Mantle 2	$(220 - d_M) \times 0.35$	7.3–8.6	4.2–4.95	3.375	Linear
Mantle 3	$(220 - d_M) \times 0.40$	7.3–8.6	4.2–4.95	3.380	Linear
220 km					
Mantle 4	70	7.5–9.6	4.4–5.2	3.480	Linear
Mantle 5	80	7.5–9.6	4.4–5.2	3.485	Uniform
Half-space	—	8.8–12.0	4.6–6.5	3.800	Uniform

Note. The thickness of the crustal layers is free to vary and is controlled by different ranges of possible bottom depths. For each geographic location, the bottom depth of the upper (lower) crustal layers is constrained by the Moho depth reported by EPcrust (d_E; Molinari & Morelli, 2011) decreased (increased) by 25%. The thickness of the first three mantle layers is determined by the Moho depth retrieved in the inversion (d_M), i.e., by the bottom depth of the lower crust, and is calculated as indicated in this table. The fourth and fifth mantle layers, below 220 km, have constant thicknesses. Within each layer, density is kept constant (and therefore not inverted for).

in our data set, and subsequent large separation between the pairs of receivers covering these regions. However, the resolution in these regions increases quickly at longer periods, resulting in an almost perfect retrieval of the synthetic model already at 13 s.

4. Inversion to Shear-Wave Velocity

We used the phase-velocity maps to derive a 3-D V_S model of the central-western Mediterranean. To do that, we first interpolated linearly their values on a regular grid with cells of 0.25° × 0.20°, so as to homogenize the spatial parameterization at all periods for both Love and Rayleigh. We then used the resulting maps, each of which consisting of 4,050 cells, to obtain an equal number of 1-D phase-velocity profiles; these were inverted for V_S using the neighborhood algorithm (e.g., Sambridge, 1999) developed by Wathelet et al. (2004) and Wathelet (2008). The neighborhood algorithm builds on a stochastic search for the layered model of Earth's parameters (i.e., V_S, P wave velocity V_P, and density) that best fit the data. In practice, the inversion is set up specifying the number of layers, their bottom depth or thickness (for which we invert for), and, for each layer, the velocity ranges within which V_S and V_P are allowed to vary. Within each layer, we assume a constant density as its impact on surface-wave dispersion can be considered negligible (e.g., Wathelet, 2005).

In a potentially infinite number of different, reasonable parameterizations, and after experimenting with several other options, we adopted an eight-layer parameterization overlying a homogeneous half-space, similar to Kästle et al. (2018); this is illustrated in Table 1. To account for the large lateral variations in the Moho depth across the study area (e.g., Molinari & Morelli, 2011), at each geographic location we set the maximum bottom depth of the last crustal layer to the value of EPcrust increased by 25%. EPcrust is a crustal model of the entire European plate, derived from a broad compilation of global and local seismic models, active seismic experiments, surface-wave studies, and receiver functions (Molinari & Morelli, 2011). Such a priori constraint allows us to investigate a tighter range of Moho depths than what would otherwise be required by the use of a fixed depth range. The consequent narrowing of the model space should in general benefit the inversion, directing the stochastic search for the best layered model toward geologically more realistic solutions.

For each of the 4,050 cells, we fed the algorithm with two phase-velocity profiles (one for Rayleigh, one for Love), that are used jointly to retrieve the best-fitting layered model. To avoid numerical instabilities in the inversion, the phase velocities are first smoothed with a running average; this operation is also motivated by the fact

that surface waves are sensitive to broad depth ranges, depending on period, that make any abrupt velocity jump unrealistic. The search for the best-fitting model is carried out iteratively, minimizing the misfit

$$\phi = \sqrt{\sum_i^n \frac{(d_i - s_i)^2}{n\, d_i^2}} \tag{2}$$

(Wathelet et al., 2004) between the true dispersion curve d (of n samples) and the synthetic one s, calculated forwardly through the investigated model. Two values of ϕ are calculated at each iteration (one for Rayleigh and one for Love), and their average drives the research in the regions of the model space characterized by the lowest misfits. Similar to Kästle et al. (2018), in this calculation, we attributed higher weights to Rayleigh-wave misfits (1 versus 0.8), due to the larger uncertainties associated with our Love measurements (see Figure 3 and Figure S1 in Supporting Information S1).

We set up the algorithm to yield 28,000 layered models for each geographic location of our grid; in each of these cells, the final model is calculated as ensemble average of the 500 best-fitting models. The resulting values of misfit are relatively low across the whole study area, as illustrated in Figure 8.

5. Results and Discussion

In the following, we discuss our V_S model in light of the relevant geological and geodynamical literature on the study area. For convenience, we adopt the bottom depths of the lower crustal layers retrieved from the inversion (see Table 1) as a proxy for the Moho depth. This allows us to separate the discussion on the shallower part of our model (Section 5.1) from that of its deeper part (Section 5.2). For illustration purposes, we show the lateral variations of such proxy in Figure 9.

Our proxy for the Moho depth is in general agreement with previous surface-wave studies (see, e.g., Figure 3d in Manu-Marfo et al. (2019)). In the region of the study area that can be considered well constrained by the data (i.e., the grid cells that have not been blanked in Figure 9, based on a visual inspection of the reconstruction tests in Figure 7), we find such proxy to be highly correlated with the values of Moho depth reported by EPcrust (Molinari & Morelli, 2011). Here, we observe a Pearson correlation coefficient of 0.91 and average differences of -1.05 ± 3.80 km. We remind the reader, however, that the values of Moho depth reported in Figure 9 should be treated with caution, since surface waves are well known to have only limited sensitivity to abrupt discontinuities (e.g., Bodin et al., 2012; Lebedev et al., 2013; Molinari & Morelli, 2011). This is especially true in correspondence of oceanic basins and/or mid-oceanic ridges, where the serpentinization of mantle rocks can represent a complicating factor by reducing the otherwise strong velocity contrast between the sedimentary cover and the metamorphosed mantle terrains. A joint analysis of surface-wave dispersion curves and deep-seismic-sounding (DSS) data may mitigate this problem, by yielding an additional constraint on the V_P/V_S ratios at those locations where DSS data are available (El-Sharkawy et al., 2021).

We show in Figure 10 several horizontal slices of our V_S model. Cross-sections of the relatively shallow and deep portions of the model are illustrated in Figures 11 and 12, respectively.

5.1. Shallow Structure

5.1.1. Liguro-Provençal Basin

The improved coverage and depth penetration of our data provide several insights into the velocity structure of this extensional basin, integrating the sparse, high-resolution studies that focused on the shallowest portion of its crust (e.g., Dannowski et al., 2020; Leroux et al., 2017). At 8-km depth, the Liguro-Provençal basin presents very low velocities, similar to those encountered mainland in the Po Plain, suggesting the presence of a thick sedimentary overburden (Figure 11, profiles AA′ and CC′). These deposits show a rather uniform thickness and correspond to the products of the syn-rift and post-rift depositional phases that occurred from the Oligocene through the Quaternary (Bache et al., 2010).

At larger depths (see slice at 11 km in Figure 10), low, typically crustal shear-wave velocities are encountered in the north-eastern part of the Liguro-Provençal basin (west of Corsica). (Compare the V_S at 11 km in the
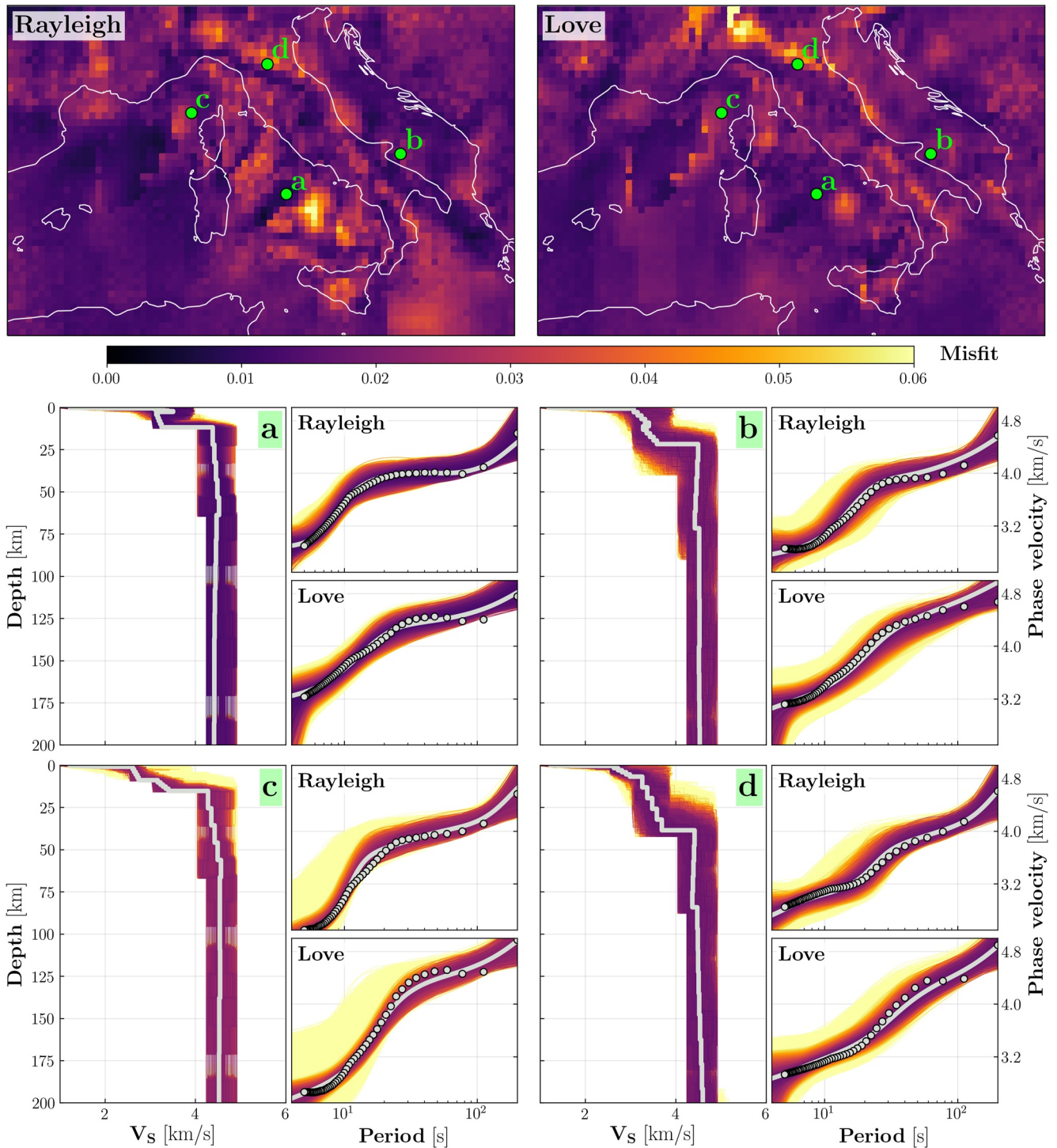
Figure 8. (top) Spatial variations of Rayleigh and Love misfit associated with the best layered models obtained through the neighborhood algorithm (Section 4). (bottom) Forwardly computed dispersion curves (right) associated with each of the 28,000 V_S models (left) investigated in the inversion; these are shown for four different locations (a, b, c, d). In each subpanel, the gray solid lines indicate the final best-fitting model, obtained by ensemble averaging the best 500 models, and its related Rayleigh and Love dispersion curves. The gray dots plotted together with the synthetic dispersion curves represent the true data points inverted by the algorithm. All subpanels share the same color palette, indicating the misfit calculated as in Equation 2.
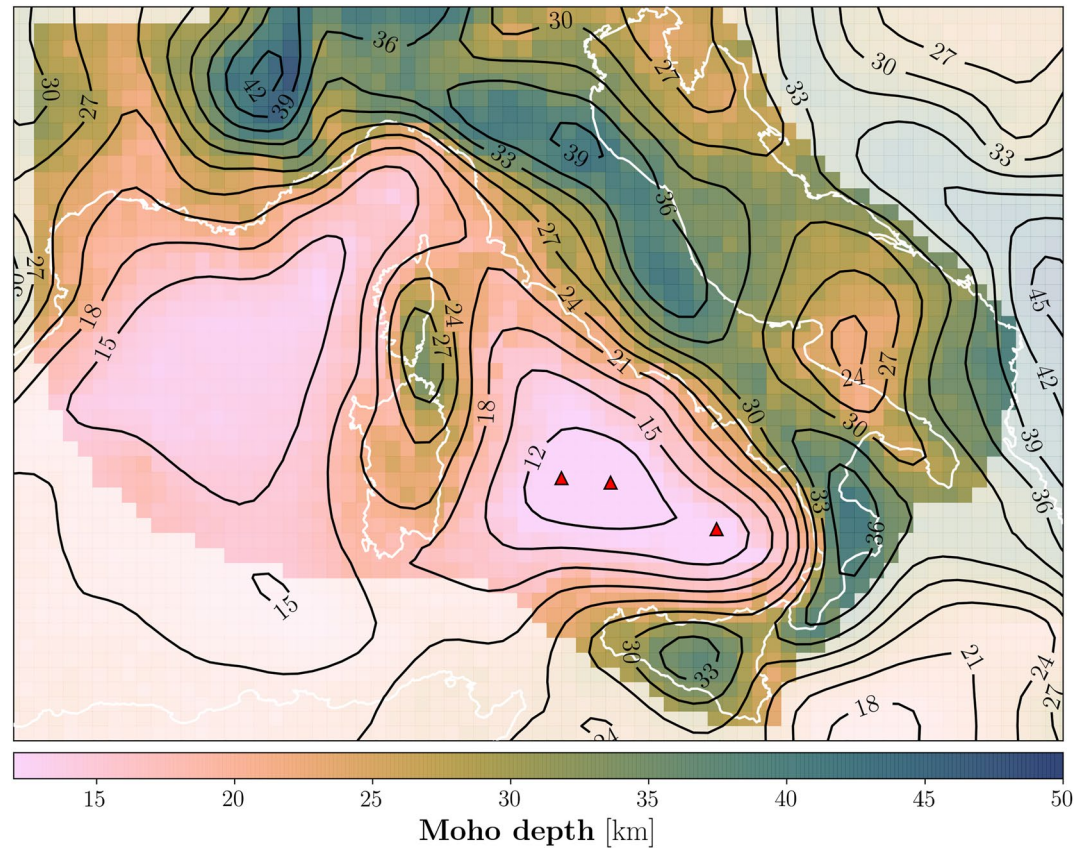
Figure 9. Depth map of Moho proxy as inferred from our 3-D V_s model. In black, the smoothed version of the Moho in the form of depth-isolines, obtained through a 2-D Gaussian filter. Red triangles indicate the Magnaghi, Vavilov, and Marsili seamounts, as illustrated in Figure 1.

Liguro-Provençal basin with those in Sardinia and in the Ligurian basin—north of Corsica.) A similar observation was reported by Dannowski et al. (2020), suggesting that this part of the basin mainly consists of a stretched crustal domain. For this reason, Dannowski et al. (2020) proposed a "failed-rift" scenario for this area, as opposed to the rest of the basin that reached a much higher overall extension, lithospheric break-up, and oceanization (De Voogd et al., 1991; Le Douaran et al., 1984; Pascal et al., 1993).

Based on the above argument, Dannowski et al. (2020) also surmised that the continent-ocean transition should be located toward the central part of the Liguro-Provençal basin (approximately south-west of Corsica, as schematically indicated in the slice at 11 km of Figure 10). Near this region, the bottom of the sedimentary cover is marked by an increase in velocities, with a bulging-upward seismic discontinuity that deepens toward the margin of the basin (see Figure 11, profile AA′). This peculiar structure can be seen as the evidence of lower crustal and upper mantle exhumation, as already pointed out in the existing literature (see Jolivet et al., 2015, and references therein). In fact, the large amount of extension in the Liguro-Provençal basin must have been accommodated by low-angle décollement surfaces (Jolivet et al., 2015), leading to the complete unroofing of the upper mantle and pronounced serpentinization.

In our model, we find that the relatively high velocities below the sedimentary cover in the central part of the Liguro-Provençal basin are, in absolute value, lower than or close to those of a typically continental domain in the same depth range (compare the Liguro-Provençal basin with Sardinia and/or Calabria in the cross-section AA′ in Figure 11, or with the Ligurian basin in the cross-section CC′). This is consistent with a relatively large thickness of serpentinized upper mantle, which has been estimated to be in the order of ∼5–7 km for this region (Jolivet et al., 2015). Moreover, the higher velocities beneath the sedimentary cover in the Ligurian basin point to a low degree of serpentinization, instead (cross-section CC′ in Figure 11), as also inferred from Dannowski et al. (2020) and Wolf et al. (2021).
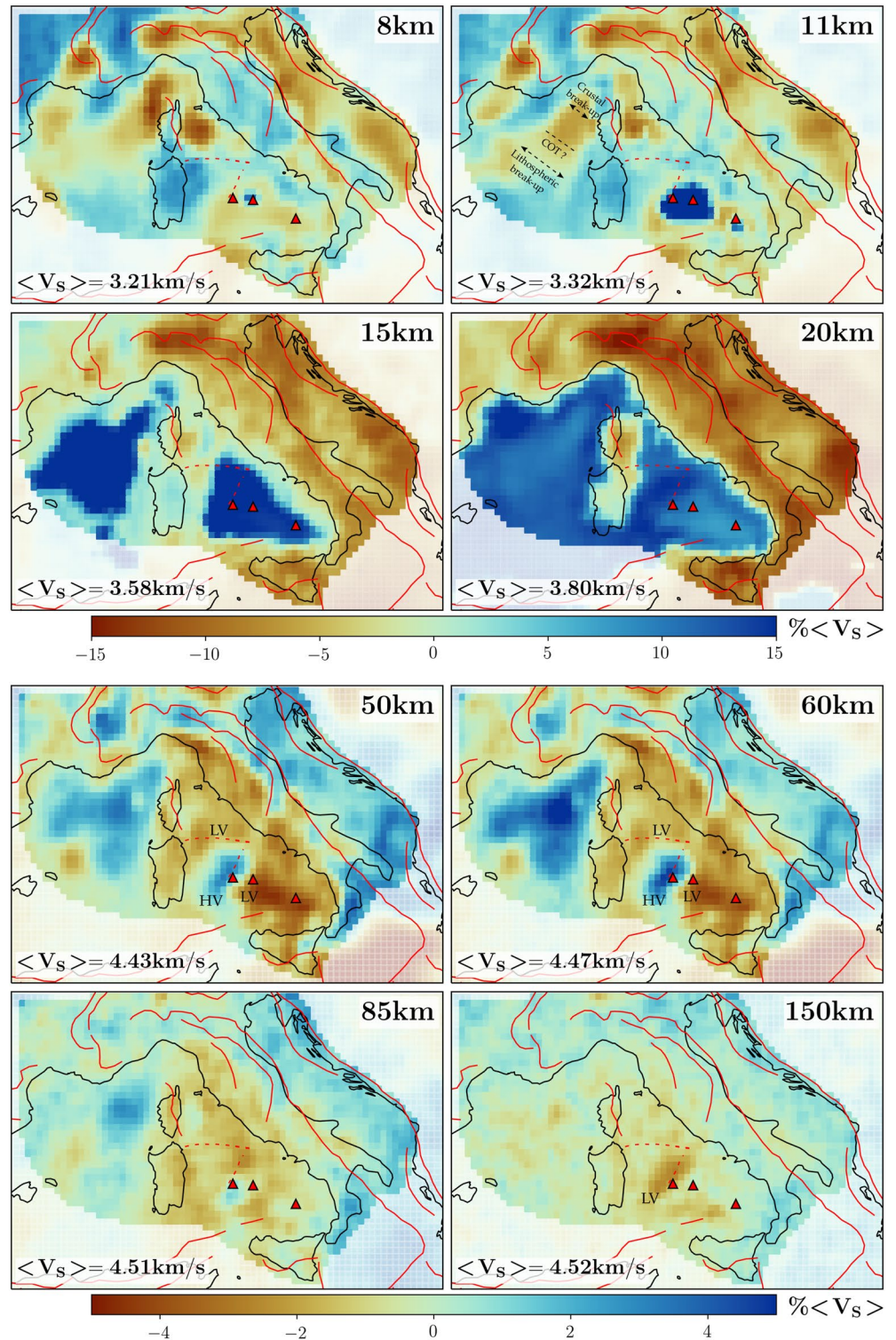
Figure 10. Shear-wave velocity maps at different depths. At each depth, the V_S values are expressed as relative variations with respect to the average, reported in the lower left of the slice. We employ two different color palettes, one for shallower depths, the other for the remaining slices. Red lines and triangles indicate the major faults across the study area and the location of the Magnaghi, Vavilov, and Marsili seamounts, as illustrated in Figure 1. The dashed black lines in the slice at 11-km depth schematically indicate the extension experienced by the Liguro-Provençal basin. In the same slice, COT indicates the approximate location of the (debated) continent-ocean transition (Dannowski et al., 2020). LV and HV point to the low and high velocities found in the Tyrrhenian basin at ≳50-km depth, as discussed in Section 5.2.
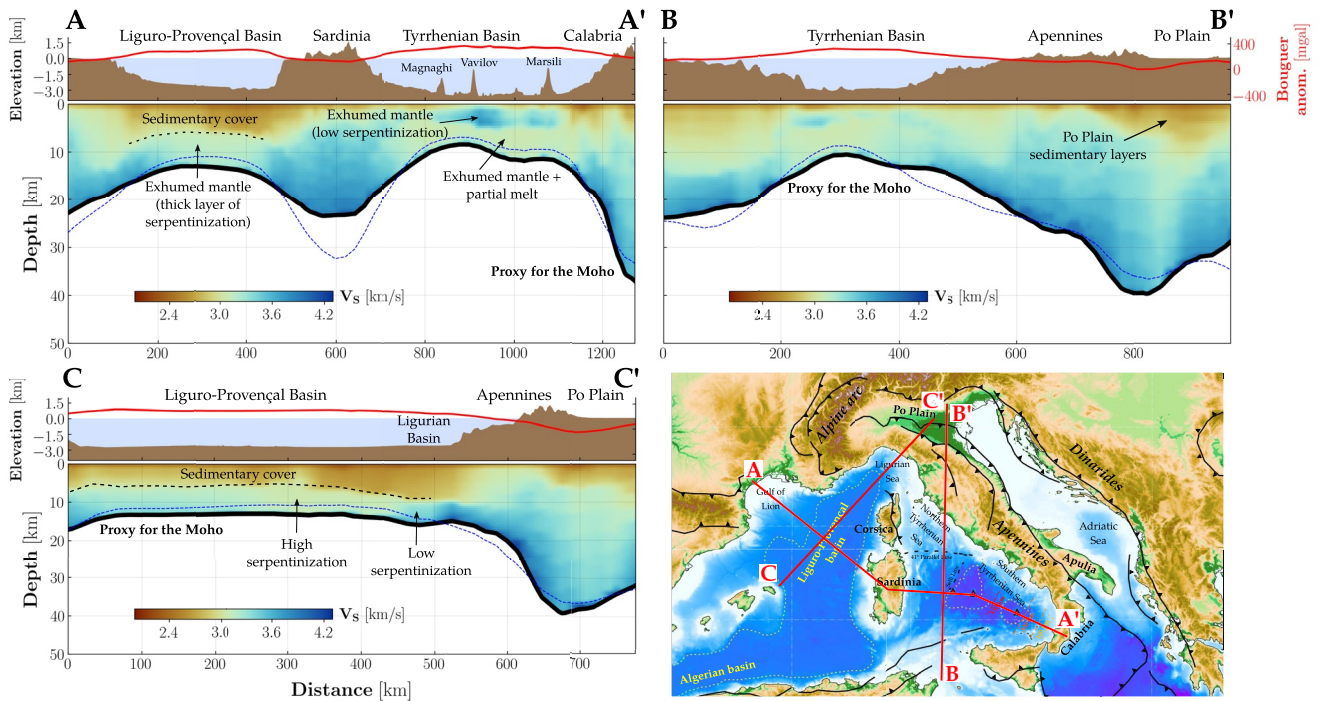
Figure 11. Shallow structure seen in three different cross-sections of the study area. The regions intersected by the profiles AA′, BB′, and CC′ are shown in the subpanel on the lower right. Topography/bathymetry is shown on the top of each cross-section, together with the Bouguer gravity anomaly (red line) as reported by Bonvalot et al. (2012). The black thick line at the bottom of each cross-section indicates our proxy for the Moho depth, whose lateral variations are illustrated in Figure 9. The blue dashed line indicates the Moho depth reported by EPcrust (Molinari & Morelli, 2011).
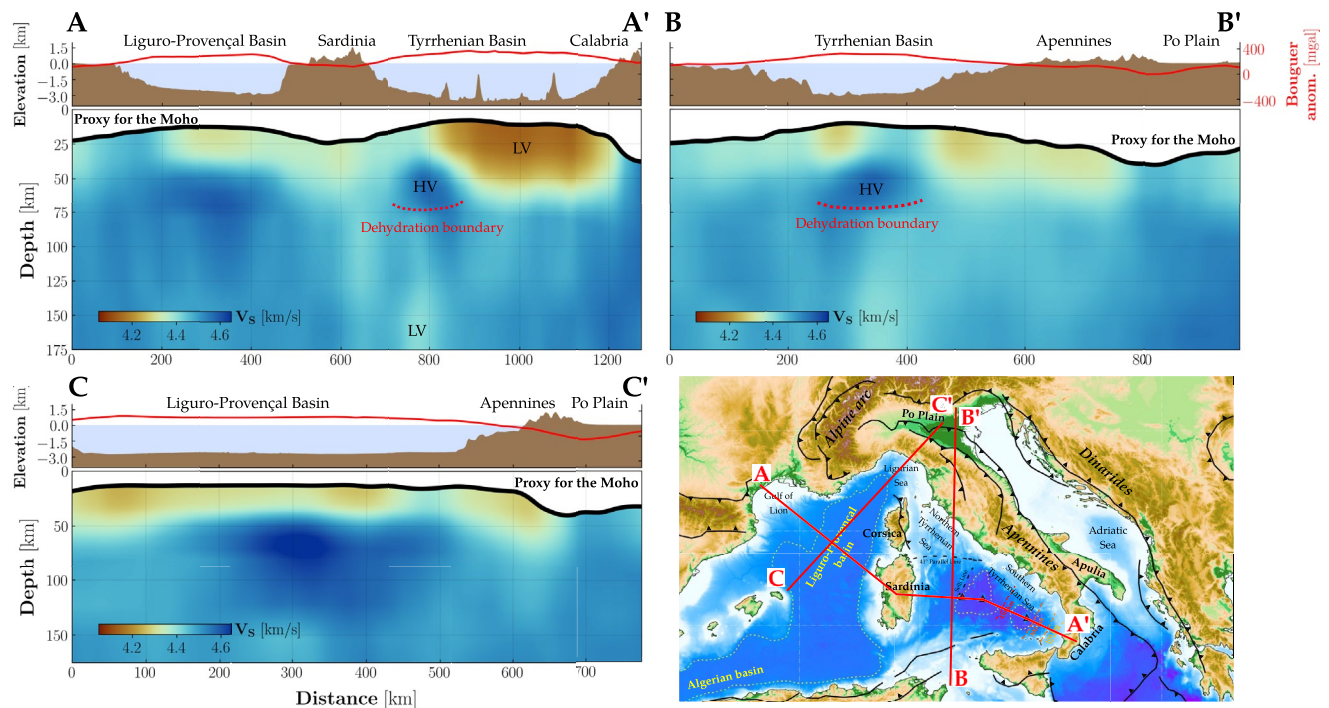

Figure 12. Same as Figure 11, but referred to the deeper part of our 3-D V_S model. LV and HV indicate the low and high velocities characterizing the strongly heterogeneous seismic structure of the Tyrrhenian basin at $\gtrsim$50-km depth, as discussed in Section 5.2.

In light of the thick layer of serpentinized mantle beneath the central part of the Liguro-Provençal basin, it is worth noting that our proxy for the Moho, as well as any other "seismic" Moho (e.g., that reported in EPcrust, Molinari & Morelli, 2011), is there unlikely to be indicative of the crust-mantle interface. Rather, it may correspond to the transition between the serpentinized and the fresh mantle underneath (Jolivet et al., 2015).

5.1.2. Tyrrhenian Basin

The seismic structure of the Tyrrhenian basin at relatively shallow depths appears rather dissimilar to that of the Liguro-Provençal basin. The vertical slice AA′ in Figure 11 indicates that, at shallow depths, higher velocities than those found in the Liguro-Provençal basin characterize the area beneath Vavilov, Magnaghi, and Marsili, pointing to the lack of any appreciable sedimentary cover. This is also confirmed by drilling surveys (Kastens & Mascle, 1990).

The high P wave velocities observed in high-resolution reflection and refraction data (Prada et al., 2014) indicate that the area surrounding the two seamounts right underneath the very thin sedimentary cover (at depths that are not well resolved in this study) is likely composed of exhumed mantle that must have reached a very high degree of serpentinization (~80%). The strong (positive) velocity gradient observed by Prada et al. (2014) also indicate that the amount of serpentinization rapidly decreases with depth, reaching ~20% in <2 km. This evidence suggests that the high velocities visible at ~5-km depths in Figure 11 (profile AA′) likely correspond to this portion of exhumed upper mantle, characterized by a low degree of serpentinization.

One distinctive feature of the seismic structure of the Tyrrhenian basin consists of a velocity inversion across most of the basin at ~6-km depth. In fact, the above high velocities are underlaid by lower seismic velocities that endure up to our proxy for the Moho depth (see profile AA′ in Figure 11). We ascribe such relatively low velocities to the presence of stagnating partial melt, which is likely connected to the episodic magmatic activity in the basin. The magmatism of the Tyrrhenian Sea is well documented and confirmed by a variety of geological, petrological, and geophysical evidence. High heat flow (>150 mW/m^2; Della Vedova et al., 2001) and geothermal gradient (>50–60 °C/km; Diaferia et al., 2019) have been observed in the basin. Ocean-drilling campaigns (Barberi et al., 1978; Bonatti et al., 1990; Dietrich et al., 1978) indicate the presence of a variety of volcanic rocks of mantle origin with different petrological characteristics, ranging from mid-oceanic ridge to ocean-island and arc-type basalts. Such heterogeneity has been explained by a complex interplay of melting and mantle contamination processes, rooted in the peculiar evolution of this extensional basin (Peccerillo, 2017).

Our proxy for the Moho indicates that mantle velocities are encountered at shallower depths than in the Liguro-Provençal basin, where, in fact, an overall lower gravity anomaly is observed (see AA′ profile in Figure 11). This is reflected by the relatively high velocities characterizing the Tyrrhenian basin in the depth slices at 8 and 11 km (Figure 10). At 8-km depth, these are approximately centered around the Vavilov seamount, and rapidly extend to the Magnaghi volcano at 11 km. In the depth range in question, such velocities are the highest found in the study area and can be seen as the evidence of a widespread "oceanization." At larger depths (15 and 20 km in Figure 10), mantle velocities (>4.1 km/s, see also Figure 12) cover most of both the Tyrrhenian and Liguro-Provençal basin.

Interestingly, in the depth slice at 11 km, also the smaller and more recent Marsili basin is distinguishable as a region characterized by relatively high velocities. This region appears separated from the larger Magnaghi-Vavilov basin by an area of relatively low velocity (Figure 10) and thicker crust (cross-section AA′ in Figure 11). This feature could be associated with the Issel Bridge, a crustal remnant of (supposedly) continental nature that has been noticed in previous studies between the Vavilov and Marsili (Doglioni et al., 2004; Sartori, 2003).

5.1.3. Apulian Region

Another shallow feature that is worth mentioning concerns the Apulian region, which is located in the south-eastern part of the Italian peninsula, adjacent to the Apennines front (Figure 1). Here, a laterally sharp high-velocity anomaly is clearly distinguishable at 8 km (Figure 10), and defines the extent of the Adria microplate. This continental anomaly corresponds to a Meso-Cenozoic carbonate succession, whose thickness ranges from 6 to 7 km (e.g., Anderson & Jackson, 1987; Channell et al., 1979; D'argenio & Horvath, 1984) and that constitutes the foreland of the southern Apennine fold-and-thrust belt (Mariotti & Doglioni, 2000). The absolute V_S we obtained in this region turn out to be in excellent agreement with those of Amato et al. (2014), calculated from broadband receiver-function inversion. Moreover, to the south-west of this region, we observe relatively low V_S in

correspondence of the southern Apennines foredeep. These velocities can be explained by the sedimentary infill of the Bradanic trough (the Pliocene-present-day south Apennines foredeep, e.g., Tropeano et al., 2002), overlaying the gently dipping carbonatic succession of the Adriatic Plate (Mariotti & Doglioni, 2000).

5.2. Deep Structure

In comparison to its shallower part, the deep part of our model (depth >40 km) shows relatively small lateral variations in V_S, that tend to decrease with increasing depth. In the continental area, relatively low velocities characterize the lithospheric mantle beneath Sardinia and Corsica (Figure 10), as opposed to the Alpine and Apennine chains, confirming previous observations by Magrini et al. (2020b).

The Tyrrhenian basin presents, on average, lower V_S compared to the Liguro-Provençal basin, and a more heterogeneous structure. Its most important feature, visible in the horizontal slices at 50 and 60 km, is the relatively high V_S in the vicinity of the Magnaghi seamount (Figure 10). This is surrounded by lower velocities, which are particularly low to the south-east of the high-velocity region (south of the Vavilov seamount) and in correspondence of the 41° Parallel line. At larger depths (Figures 10 and 12), the high velocities delineating this peculiar structure disappear, and are replaced by relatively low velocities which are, on average, ~2% lower than those found in the Liguro-Provençal basin, in the Ionian and in the Adriatic Sea (see the horizontal slices at 85 and 150 km in Figure 10).

A similar seismic structure in the Tyrrhenian basin has already been observed by Greve et al. (2014), and interpreted as a portion of high-velocity, dehydrated mantle related to the formation of oceanic crust in the same region. Owing to a better seismic coverage, however, our model provides improved spatial constraints on the location and depth-range (~50–75 km) spanned by the relatively high V_S defining such strong lateral heterogeneities (Figures 10 and 12). In fact, while in Greve et al. (2014), the high-velocity region was characterized by a rather equidimensional shape (circular in the horizontal slice) and covered most of the Vavilov-Magnaghi basin (see their Figures 5 and 7), we find it elongated toward SSW-NNE, and mostly located to the north and west of the Magnaghi seamount. Notably, we find this structure to be aligned with the Selli line, and bounded (to the north) by the 41° Parallel morpho-tectonic lineament (Figure 10).

5.2.1. Ionian Slab Retreat and Mantle Heterogeneity

The subduction-related mantle flow can determine the evolution of back-arc basins and the extent of the associated volcanism (e.g., Magni, 2019). Together with mantle flow, the deep-water cycle in the "subduction factory" is another key ingredient. In fact, while most of subduction-related water is released through arc volcanism, a significant fraction is transported at depth and stored in minerals' crystal structures (i.e., in dense hydrous magnesium-silicates and nominally anhydrous minerals, Ferot & Bolfan-Casanova, 2012; Nakagawa et al., 2015). As a consequence, "flux melting" (i.e., the fluid-induced melting process typical of volcanic arcs, e.g., Iwamori, 1992) can also be observed in back-arc basins, such as the Tyrrhenian Sea (Trua et al., 2007).

The formation of the Tyrrhenian basin can be ascribed to the (ongoing) dynamics of subduction, narrowing, and tearing of the Ionian slab; this has been the focus of geodynamic modeling by several authors (e.g., Faccenna et al., 2007; Rosenbaum et al., 2008; Wortel & Spakman, 2000) and is still matter of debate. The volatiles' chemical signature and the highly heterogeneous character of the basalts sampled in the southern Tyrrhenian basin (Trua et al., 2007) point to a lateral mantle flow approximately directed SW-NE beneath this back-arc region, from the western margin of the Ionian slab. This was likely triggered by the Ionian slab tearing and detachment, as substantiated by both seismological (shear-wave splitting and anisotropy) and structural studies (see Faccenna et al., 2014, and references therein).

In recent times, an effort has been made to reconcile active seismic observations with those collected in ocean drilling surveys, that resulted in a detailed tectonic map of the Tyrrhenian Sea and in a new kinematic model for the opening of the basin (see Loreto et al., 2021, and references therein). According to Loreto et al. (2021), the formation of the Magnaghi basin can be traced back to the crustal thinning started ~12.5 Ma, followed by an extensional phase from ~11 to ~6 Ma. Afterward (~5 Ma, in the Pliocene), a new, rapid extensional phase in the southern Tyrrhenian basin, approximately oriented NW-SE and accompanied by extensive intraplate volcanism, caused the opening of the Vavilov basin. Loreto et al. (2021) ascribe this more recent episode to the rapid retreat

of the Ionian slab and to the lateral mantle inflow induced by the slab break-off, consistent with previous geodynamic interpretations (e.g., Faccenna et al., 2007; Rosenbaum & Lister, 2004).

Our V_S model confirms the above hypothesis. The low velocities found in the south-eastern part of the Tyrrhenian basin at 50–60 km (Figures 10 and 12) can be explained by the prominent mantle inflow from the edges of the Ionian slab, that is likely to be associated with a conspicuous presence of fluids and/or melt. We also find particularly low velocities along the 41° Parallel line, which we interpret as a region characterized by high fluid content due to the intrusion of mantle material during the rapid Pliocenic extension. On the contrary, the high-velocities found in the north-western margin of the Tyrrhenian basin at the same depths, which can be seen as the midportion of a "ring-shaped" structure (Greve et al., 2014), are indicative of a "dry" portion the upper mantle. We speculate that this portion of the basin was not affected by as prominent a mantle flow as the rest of the Tyrrhenian basin, because it was formed before the rapid extension due to the Ionian slab break-off (i.e., before the Pliocene phase described in Loreto et al. (2021)).

5.2.2. Mantle Dehydration Boundary

The formation of oceanic crust requires melt extraction from the mantle. In principle, the mechanisms governing such process can involve either "decompression melting" (as in mid-ocean ridges) or flux melting (in regions characterized by an extensive presence of fluids, like volcanic arcs). Karato (1986) postulated that, whenever the main process for the formation of oceanic crust involves decompression melting, a dehydration boundary separating the more hydrated portion of the mantle from its overlying (and relatively dry) counterpart should be observed. The arguments brought forth by Karato (1986) were then substantiated by Karato (2008), and finally supported by the seismic imaging of mid-ocean ridges (e.g., Cammarano et al., 2011; Goes et al., 2012). A similar process of dehydration can also occur in back-arc basins, as evidenced by the strong similarity of their volcanic products to those found in the mid-oceanic ridges (e.g., Kelley et al., 2006).

In our model, we find that the high velocities characterizing the north-western portion of the Tyrrhenian basin (visible in Figure 10 at 50-km and 60-km depth) rapidly vanish at ∼70–75-km depth, and are replaced by relatively low velocities at larger depths (Figures 10 and 12). These are ∼2% lower than those found in the rest of the basin and in the Liguro-Provençal basin at the same depths. Consistent with the presence of a dehydration boundary, we interpret this change in velocity with depth as a compositional change in terms of water content, triggered by a mechanism of decompression melting, from a deep and hydrated mantle to a shallower and dry one.

Greve et al. (2014) gave a similar interpretation for the relatively high velocities they found in most of the Tyrrhenian basin, implying that its "oceanization" lead to a dry and fast mantle portion approximately below the Vavilov seamount. Owing to a better resolution, we revise here their interpretation. In fact, it appears from our model that only the prepliocene portion of the Tyrrhenian basin (west of the Magnaghi seamount) presents such structure, while the remaining part of the basin is characterized by lower velocities likely linked to the mantle inflow due to slab-dynamics processes.

It is worth noting that the relatively high velocities in the Tyrrhenian basin at 50–60 km are, in absolute value, similar to those found in most of the Liguro-Provençal basin at the same depths (Figure 10), but no dehydration boundary is observed in the latter at larger depths. We speculate that (a) similar mechanisms of melt extraction (i.e., decompression melting) have characterized the two regions in their evolution, and (b) the Liguro-Provençal basin is characterized by a lower concentration of fluids (hence, the elusive dehydration boundary) at relatively large depths (≳70–75 km).

At depths ≳70–75 km, most of the Tyrrhenian basin has ∼2% lower velocities than those found in the Liguro-Provençal basin at the same depths (Figure 10). Once again, the difference can be in principle ascribed to a greater concentration of fluids in the Tyrrhenian basin. An alternative explanation would involve the role of temperature. Based on receiver functions, Monna et al. (2019) showed that the Tyrrhenian mantle is characterized by a thinning of the 410–660 transition zone, possibly associated with relatively high temperatures. From thermodynamic modeling, relative differences of ∼2% in V_S can be ascribed, in the first approximation, to temperature variations of ∼200°C (e.g., Cammarano & Guerri, 2017; Cammarano et al., 2003). This would imply higher temperatures in the Tyrrhenian basin (compared to the Liguro-Provençal basin) at depths ≳70–75 km, which in principle would be consistent with the results of Monna et al. (2019).

Although we cannot rule out the contribution of temperature to the low velocities at relatively large depths in the Tyrrhenian basin, the highly heterogeneous mantle structure of this basin, shown in our study and expected from recent kinematics models (Loreto et al., 2021), points to the prominent role of fluids in controlling its seismic structure. Our interpretation implies that slab dynamics can control shallow extensional processes as well as the compositional and mineralogical character of the upper mantle in back-arc basins.

6. Conclusions

We derived a new 3-D shear-wave velocity (V_S) model of the central-western Mediterranean. To do that, we relied on the LiSard array, a new seismic array deployed on the Sardinia Island, and on all the publicly available seismograms from southern Europe and northern Africa. Based on 807 receivers, we first retrieved Rayleigh and Love interstation phase velocities, exploiting 3,823 teleseismic earthquakes (EQ) and continuous recordings of seismic ambient noise (AN). We then translated the dispersion curves into phase-velocity maps, using a linear-least-squares inversion algorithm based on the ray theory. Owing to the larger number of interstation paths covering the oceanic regions, the maps display enhanced resolution in comparison with previous studies, especially in the Liguro-Provençal and in the Tyrrhenian basin. Finally, we used the phase-velocity maps to obtain 4,050 phase-velocity profiles, extracted at each grid point of a regular grid covering the study area. Those were nonlinearly inverted for the 3-D V_S structure of the study area, using the neighborhood algorithm.

As opposed to the Tyrrhenian basin, we found evidence of a widespread sedimentary cover in the Liguro-Provençal basin at shallow depths (<11 km), associated with relatively low velocities. At ∼5-km depth, relatively high velocities are found below the Tyrrhenian basin, consistent with the presence of an exhumed mantle characterized by a low degree of serpentinization. At larger depths (up to the Moho depth), such high velocities are replaced by lower velocities, which we interpreted in terms of stagnating partial melt probably linked to the surface volcanism experienced by the region. At 11-km depth, the highest velocities in the study area are approximately centered around the Magnaghi-Vavilov and Marsili basin, due to an even shallower Moho and consistent with the (ongoing) oceanization of the Tyrrhenian basin.

At depths >50 km, the most prominent feature of our model is a strongly heterogeneous structure in the Tyrrhenian basin, with relatively high velocities characterizing the north-western portion of the basin. We found these high velocities to be approximately aligned with the Selli line, bounded (to the north) by the 41° Parallel line, and surrounded by anomalously low velocities. We ascribed the high velocities characterizing this structure to a dehydrated portion of the upper mantle, which we related to the formation of oceanic crust in the same region by decompression melting. On the contrary, consistent with recent geodynamics and kinematics modeling, we interpreted the lower velocities found in the rest of the basin as the evidence of a conspicuous presence of fluids (due to a pronounced mantle inflow from the edges of the Ionian slab), which has likely favored the surface volcanism through flux melting.

The above structure in the Tyrrhenian basin disappears at larger depths and is replaced by relatively low velocities, which are ∼2% lower than those found in the Liguro-Provençal basin and in the Adriatic Sea at the same depths. This rapid change in velocity with depth delineates a dehydration boundary, which we identified at ∼70–75-km depth, separating the more hydrated portion of the mantle from its overlying (and relatively dry) counterpart. Based on the lack of evidence of such boundary in the Liguro-Provençal basin, we also inferred that, compared to the Tyrrhenian, the Liguro-Provençal basin is characterized by an overall smaller concentration of fluids at depths ≳70–75 km.

Our model provides evidence that the physical conditions of back-arc basins are governed by subduction-related dynamics. Extensive presence of fluids and relatively high temperatures can shape the geodynamical evolution of back-arc basins, by controlling the rheology of the crust and lithospheric mantle.

Data Availability Statement

We used publicly available seismic data from the EIDA archive (http://www.orfeus-eu.org/eida).

References

Aki, K. (1957). *Space and time spectra of stationary waves with special reference to microtremors* (Vol. 35, pp. 415–456). Bulletin of the Earthquake Research Institute, University of Tokyo.

Amato, A., Bianchi, I., & Agostinetti, N. P. (2014). Apulian crust: Top to bottom. *Journal of Geodynamics*, *82*, 125–137.

Anderson, H., & Jackson, J. (1987). Active tectonics of the Adriatic region. *Geophysical Journal International*, *91*(3), 937–983.

Bache, F., Olivet, J. L., Gorini, C., Aslanian, D., Labails, C., & Rabineau, M. (2010). Evolution of rifted continental margins: The case of the gulf of lions (western Mediterranean basin). *Earth and Planetary Science Letters*, *292*(3–4), 345–356.

Barberi, F., Bizouard, H., Capaldi, G., Ferrara, G., Gasparini, P., Innocenti, F., et al. (1978). Age and nature of basalts from the Tyrrhenian abyssal plain. *Initial Reports of the Deep Sea Drilling Project*, *42*, 509–514.

Bodin, T., Sambridge, M., Tkalčić, H., Arroucau, P., Gallagher, K., & Rawlinson, N. (2012). Transdimensional inversion of receiver functions and surface wave dispersion. *Journal of Geophysical Research*, *117*, B02301. https://doi.org/10.1029/2011JB008560

Bonatti, E., Seyler, M., Channell, J., Girardeau, J., & Mascle, G. (1990). Peridotites drilled from the Tyrrhenian Sea, ODP leg 107. *Proceedings of the Ocean Drilling Program, Scientific Results*, *107*, 37–47.

Bonvalot, S., Balmino, G., Briais, A., Kuhn, M., Peyrefitte, A., Vales, N., et al. (2012). *World gravity map*. Bureau Gravimetrique International (BGI), Map, CGMW-BGI-CNES728IRD.

Boschi, L., & Dziewonski, A. M. (1999). High-and low-resolution images of the Earth's mantle: Implications of different approaches to tomographic modeling. *Journal of Geophysical Research*, *104*(B11), 25567–25594.

Boschi, L., Magrini, F., Cammarano, F., & van der Meijde, M. (2019). On seismic ambient noise cross-correlation and surface-wave attenuation. *Geophysical Journal International*, *219*(3), 1568–1589.

Boschi, L., Magrini, F., Cammarano, F., & van der Meijde, M. (2020). Erratum: On seismic ambient noise cross-correlation and surface-wave attenuation. *Geophysical Journal International*, *222*(2), 1090–1092.

Cammarano, F., Goes, S., Vacher, P., & Giardini, D. (2003). Inferring upper-mantle temperatures from seismic velocities. *Physics of the Earth and Planetary Interiors*, *138*(3–4), 197–222.

Cammarano, F., & Guerri, M. (2017). Global thermal models of the lithosphere. *Geophysical Journal International*, *210*(1), 56–72.

Cammarano, F., Tackley, P., & Boschi, L. (2011). Seismic, petrological and geodynamical constraints on thermal and compositional structure of the upper mantle: Global thermochemical models. *Geophysical Journal International*, *187*(3), 1301–1318.

Channell, J., D'argenio, B., & Horvath, F. (1979). Adria, the African promontory, in Mesozoic Mediterranean palaeogeography. *Earth-Science Reviews*, *15*(3), 213–292.

Chiarabba, C., & Palano, M. (2017). Progressive migration of slab break-off along the southern Tyrrhenian plate boundary: Constraints for the present day kinematics. *Journal of Geodynamics*, *105*, 51–61.

Dannowski, A., Kopp, H., Grevemeyer, I., Lange, D., Thorwart, M., Bialas, J., & Wollatz-Vogt, M. (2020). Seismic evidence for failed rifting in the Ligurian Basin, Western Alpine Domain. *Solid Earth*, *11*(3), 873–887.

D'argenio, B., & Horvath, F. (1984). Some remarks on the deformation history of Adria, from the Mesozoic to the Tertiary. *Annales Geophysicae*, *2*, 143–146.

De Voogd, B., Nicolich, R., Olivet, J., Fanucci, F., Burrus, J., Mauffret, A., et al. (1991). First deep seismic reflection transect from the Gulf of Lions to Sardinia (ECORS-CROP profiles in western Mediterranean). In *Continental lithosphere: Deep seismic reflections* (Vol. 22, pp. 265–274).

Della Vedova, B., Bellani, S., Pellis, G., & Squarci, P. (2001). Deep temperatures and surface heat flow distribution. In *Anatomy of an orogen: The Apennines and adjacent Mediterranean basins* (pp. 65–76). Springer.

Diaferia, G., Cammarano, F., & Faccenna, C. (2019). Thermal structure of a vanishing subduction system: An example of seismically-derived crustal temperature along the Italian peninsula. *Geophysical Journal International*, *219*(1), 239–247.

Dietrich, V., Emmermann, R., Puchelt, H., & Keller, J. (1978). *Oceanic basalts from the Tyrrhenian basin, DSDP Leg 42A, Hole 373A*.

Doglioni, C., Innocenti, F., Morellato, C., Procaccianti, D., & Scrocca, D. (2004). On the opening of the Tyrrhenian Sea. *Memorie Descrittive della Carta geologica d'Italia*, *44*, 147–164.

Ekström, G., Abers, G. A., & Webb, S. C. (2009). Determination of surface-wave phase velocities across USArray from noise and Aki's spectral formulation. *Geophysical Research Letters*, *36*, L18301. https://doi.org/10.1029/2009GL039131

El-Sharkawy, A., Meier, T., Hübscher, C., Lebedev, S., Dannowski, A., Kopp, H., et al. (2021). Lithospheric structure of the eastern Mediterranean Sea: Inferences from surface wave tomography and stochastic inversions constrained by wide-angle refraction measurements. *Tectonophysics*, *821*, 229159.

El-Sharkawy, A., Meier, T., Lebedev, S., Behrmann, J., Hamada, M., Cristiano, L., et al. (2020). The slab puzzle of the Alpine-Mediterranean region: Insights from a new, high-resolution, shear-wave velocity model of the upper mantle. *Geochemistry, Geophysics, Geosystems*, *21*, e2020GC008993. https://doi.org/10.1029/2020GC008993

Faccenna, C., Becker, T. W., Auer, L., Billi, A., Boschi, L., Brun, J. P., et al. (2014). Mantle dynamics in the Mediterranean. *Reviews of Geophysics*, *52*(3), 283–332.

Faccenna, C., Becker, T. W., Lucente, F. P., Jolivet, L., & Rossetti, F. (2001). History of subduction and back arc extension in the central Mediterranean. *Geophysical Journal International*, *145*(3), 809–820.

Faccenna, C., Funiciello, F., Civetta, L., D Antonio, M., Moroni, M., & Piromallo, C. (2007). Slab disruption, mantle circulation, and the opening of the Tyrrhenian basins. *Special Papers-Geological Society of America*, *418*, 153.

Faccenna, C., Piromallo, C., Crespo-Blanc, A., Jolivet, L., & Rossetti, F. (2004). Lateral slab deformation and the origin of the western Mediterranean arcs. *Tectonics*, *23*, TC1012. https://doi.org/10.1029/2002TC001488

Faccenna, C., Speranza, F., Caracciolo, F. D., Mattei, M., & Oggiano, G. (2002). Extensional tectonics on Sardinia (Italy): Insights into the arc-back-arc transitional regime. *Tectonophysics*, *356*(4), 213–232.

Ferot, A., & Bolfan-Casanova, N. (2012). Water storage capacity in olivine and pyroxene to 14 GPa: Implications for the water content of the Earth's upper mantle and nature of seismic discontinuities. *Earth and Planetary Science Letters*, *349*, 218–230.

Fichtner, A., Stehly, L., Ermert, L., & Boehm, C. (2016). Generalised interferometry—I. Theory for inter-station correlations. *Geophysical Journal International*, *208*, 603–638.

Friedrich, A., Krüger, F., & Klinge, K. (1998). Ocean-generated microseismic noise located with the Gräfenberg array. *Journal of Seismology*, *2*(1), 47–64.

Gattacceca, J., & Speranza, F. (2002). Paleomagnetism of Jurassic to Miocene sediments from the Apenninic carbonate platform (southern Apennines, Italy): Evidence for a 60 counterclockwise Miocene rotation. *Earth and Planetary Science Letters*, *201*(1), 19–34.

Goes, S., Armitage, J., Harmon, N., Smith, H., & Huismans, R. (2012). Low seismic velocities below mid-ocean ridges: Attenuation versus melt retention. *Journal of Geophysical Research*, *117*, B12403. https://doi.org/10.1029/2012JB009637

Greve, S., Paulssen, H., Goes, S., & van Bergen, M. (2014). Shear-velocity structure of the Tyrrhenian Sea: Tectonics, volcanism and mantle (de) hydration of a back-arc basin. *Earth and Planetary Science Letters*, *400*, 45–53.

Gvirtzman, Z., & Nur, A. (1999). The formation of Mount Etna as the consequence of slab rollback. *Nature*, *401*(6755), 782–785.

Hansen, P. C. (1999). *The L-curve and its use in the numerical treatment of inverse problems*. WIT Press.

Iwamori, H. (1992). Degree of melting and source composition of Cenozoic basalts in southwest Japan: Evidence for mantle upwelling by flux melting. *Journal of Geophysical Research*, *97*(B7), 10983–10995.

Jolivet, L., Gorini, C., Smit, J., & Leroy, S. (2015). Continental breakup and the dynamics of rifting in back-arc basins: The gulf of lion margin. *Tectonics*, *34*, 662–679. https://doi.org/10.1002/2014TC003570

Karato, S. (1986). Does partial melting reduce the creep strength of the upper mantle? *Nature*, *319*(6051), 309–310.

Karato, S.-i. (2008). Deformation of Earth materials. In *An introduction to the rheology of Solid Earth* (pp. 454–463). Cambridge University Press.

Kastens, K., & Mascle, J. (1990). The geological evolution of the Tyrrhenian Sea: An introduction to the scientific results of ODP Leg 107. In *Proceedings of the Ocean Drilling Program, Scientific Results* (Vol. 107, p. 26). College Station, TX: Ocean Drilling Program.

Kästle, E., Soomro, R., Weemstra, C., Boschi, L., & Meier, T. (2016). Two-receiver measurements of phase velocity: Cross-validation of ambient-noise and earthquake-based observations. *Geophysical Journal International*, *207*, 1493–1512.

Kästle, E. D., El-Sharkawy, A., Boschi, L., Meier, T., Rosenberg, C., Bellahsen, N., et al. (2018). Surface wave tomography of the Alps using ambient-noise and earthquake phase velocity measurements. *Journal of Geophysical Research: Solid Earth*, *123*, 1770–1792. https://doi.org/10.1002/2017JB014698

Kelley, K. A., Plank, T., Grove, T. L., Stolper, E. M., Newman, S., & Hauri, E. (2006). Mantle melting as a function of water content beneath back-arc basins. *Journal of Geophysical Research*, *111*, B09208. https://doi.org/10.1029/2005JB003732

Lebedev, S., Adam, J. M.-C., & Meier, T. (2013). Mapping the Moho with seismic surface waves: A review, resolution analysis, and recommended inversion strategies. *Tectonophysics*, *609*, 377–394.

Le Douaran, S., Burrus, J., & Avedik, F. (1984). Deep structure of the north-western Mediterranean basin: Results of a two-ship seismic survey. *Marine Geology*, *55*(3–4), 325–345.

Leroux, E., Rabineau, M., Aslanian, D., Gorini, C., Molliex, S., Bache, F., et al. (2017). High-resolution evolution of terrigenous sediment yields in the provence basin during the last 6 ma: Relation with climate and tectonics. *Basin Research*, *29*(3), 305–339.

Lin, F.-C., Moschetti, M. P., & Ritzwoller, M. H. (2008). Surface wave tomography of the western United States from ambient seismic noise: Rayleigh and Love wave phase velocity maps. *Geophysical Journal International*, *173*(1), 281–298.

Loreto, M. F., Zitellini, N., Ranero, C. R., Palmiotto, C., & Prada, M. (2021). Extensional tectonics during the Tyrrhenian back-arc basin formation and a new morpho-tectonic map. *Basin Research*, *33*(1), 138–158.

Lu, Y., Stehly, L., Paul, A., & Group, A. W. (2018). High-resolution surface wave tomography of the European crust and uppermost mantle from ambient seismic noise. *Geophysical Journal International*, *214*(2), 1136–1150.

Magni, V. (2019). The effects of back-arc spreading on arc magmatism. *Earth and Planetary Science Letters*, *519*, 141–151.

Magrini, F., Diaferia, G., Boschi, L., & Cammarano, F. (2020a). Arrival-angle effects on two-receiver measurements of phase velocity. *Geophysical Journal International*, *220*(3), 1838–1844.

Magrini, F., Diaferia, G., Fadel, I., Cammarano, F., van der Meijde, M., & Boschi, L. (2020b). 3-D shear wave velocity model of the lithosphere below the Sardinia-Corsica continental block based on Rayleigh-wave phase velocities. *Geophysical Journal International*, *220*(3), 2119–2130.

Manu-Marfo, D., Aoudia, A., Pachhai, S., & Kherchouche, R. (2019). 3D shear wave velocity model of the crust and uppermost mantle beneath the Tyrrhenian basin and margins. *Scientific Reports*, *9*(1), 1–10.

Mariotti, G., & Doglioni, C. (2000). The dip of the foreland monocline in the Alps and Apennines. *Earth and Planetary Science Letters*, *181*(1–2), 191–202.

Meier, T., Dietrich, K., Stöckhert, B., & Harjes, H.-P. (2004). One-dimensional models of shear wave velocity for the eastern Mediterranean obtained from the inversion of Rayleigh wave phase velocities and tectonic implications. *Geophysical Journal International*, *156*(1), 45–58.

Molinari, I., & Morelli, A. (2011). EPcrust: A reference crustal model for the European Plate. *Geophysical Journal International*, *185*(1), 352–364.

Monna, S., Montuori, C., Piromallo, C., & Vinnik, L. (2019). Mantle structure in the Central Mediterranean Region from P and S receiver functions. *Geochemistry, Geophysics, Geosystems*, *20*, 4545–4566. https://doi.org/10.1029/2019GC008496

Nakagawa, T., Nakakuki, T., & Iwamori, H. (2015). Water circulation and global mantle dynamics: Insight from numerical modeling. *Geochemistry, Geophysics, Geosystems*, *16*, 1449–1464. https://doi.org/10.1002/2014GC005701

Pascal, G., Mauffret, A., & Patriat, P. (1993). The ocean-continent boundary in the gulf of lion from analysis of expanding spread profiles and gravity modelling. *Geophysical Journal International*, *113*(3), 701–726.

Peccerillo, A. (2017). Southern Tyrrhenian Sea. In *Cenozoic volcanism in the Tyrrhenian Sea region* (pp. 339–362). Springer.

Prada, M., Sallarès, V., Ranero, C. R., Vendrell, M., Grevemeyer, I., Zitellini, N., & de Franco, R. (2014). Seismic structure of the Central Tyrrhenian basin: Geophysical constraints on the nature of the main crustal domains. *Journal of Geophysical Research: Solid Earth*, *119*, 52–70. https://doi.org/10.1002/2013JB010527

Ritzwoller, M. H., Lin, F.-C., & Shen, W. (2011). Ambient noise tomography with a large seismic array. *Comptes Rendus Geoscience*, *343*(8–9), 558–570.

Rosenbaum, G., Gasparon, M., Lucente, F. P., Peccerillo, A., & Miller, M. S. (2008). Kinematics of slab tear faults during subduction segmentation and implications for Italian magmatism. *Tectonics*, *27*, TC2008. https://doi.org/10.1029/2007TC002143

Rosenbaum, G., & Lister, G. S. (2004). Neogene and Quaternary rollback evolution of the Tyrrhenian Sea, the Apennines, and the Sicilian Maghrebides. *Tectonics*, *23*, TC1013. https://doi.org/10.1029/2003TC001518

Sambridge, M. (1999). Geophysical inversion with a neighbourhood algorithm—II. Appraising the ensemble. *Geophysical Journal International*, *138*(3), 727–746.

Sartori, R. (2003). The Tyrrhenian back-arc basin and subduction of the Ionian lithosphere. *Episodes*, *26*(3), 217–221.

Schaefer, J., Boschi, L., & Kissling, E. (2011). Adaptively parametrized surface wave tomography: Methodology and a new model of the European upper mantle. *Geophysical Journal International*, *186*(3), 1431–1453.

Soomro, R., Weidle, C., Cristiano, L., Lebedev, S., Meier, T., & Group, P. W. (2016). Phase velocities of Rayleigh and Love waves in central and northern Europe from automated, broad-band, interstation measurements. *Geophysical Journal International*, *204*(1), 517–534.

Tropeano, M., Sabato, L., & Pieri, P. (2002). Filling and cannibalization of a foredeep: The Bradanic Trough, Southern Italy. *Geological Society, London, Special Publications*, *191*, 55–79.

Trua, T., Serri, G., & Marani, M. P. (2007). Geochemical features and geodynamic significance of the southern Tyrrhenian backarc basin. In *Cenozoic volcanism in the Mediterranean area* (Vol. 418, pp. 221).

Wathelet, M. (2005). *Array recordings of ambient vibrations: Surface-wave inversion (PhD dissertation)*. Liége University.

Wathelet, M. (2008). An improved neighborhood algorithm: Parameter conditions and dynamic scaling. *Geophysical Research Letters*, *35*, L09301. https://doi.org/10.1029/2008GL033256

Wathelet, M., Jongmans, D., & Ohrnberger, M. (2004). Surface-wave inversion using a direct search algorithm and its application to ambient vibration measurements. *Near Surface Geophysics*, *2*(4), 211–221.

Wolf, F. N., Lange, D., Dannowski, A., Thorwart, M., Crawford, W., Wiesenberg, L., et al. (2021). 3D crustal structure of the Ligurian Basin revealed by surface wave tomography using ocean bottom seismometer data. *Solid Earth*, *12*(11), 2597–2613.

Wortel, M., & Spakman, W. (2000). Subduction and slab detachment in the Mediterranean-Carpathian region. *Science*, *290*(5498), 1910–1917.

Zhou, L., Xie, J., Shen, W., Zheng, Y., Yang, Y., Shi, H., & Ritzwoller, M. H. (2012). The structure of the crust and uppermost mantle beneath South China from ambient noise and earthquake tomography. *Geophysical Journal International*, *189*(3), 1565–1583.